nature cancer

Article

https://doi.org/10.1038/s43018-023-00556-5

GAP43-dependent mitochondria transfer from astrocytes enhances glioblastoma tumorigenicity

Received: 14 December 2022

Accepted: 6 April 2023

Published online: 11 May 2023

Check for updates

A list of authors and their affiliations appears at the end of the paper

The transfer of intact mitochondria between heterogeneous cell types has been confirmed in various settings, including cancer. However, the functional implications of mitochondria transfer on tumor biology are poorly understood. Here we show that mitochondria transfer is a prevalent phenomenon in glioblastoma (GBM), the most frequent and malignant primary brain tumor. We identified horizontal mitochondria transfer from astrocytes as a mechanism that enhances tumorigenesis in GBM. This transfer is dependent on network-forming intercellular connections between GBM cells and astrocytes, which are facilitated by growth-associated protein 43 (GAP43), a protein involved in neuron axon regeneration and astrocyte reactivity. The acquisition of astrocyte mitochondria drives an increase in mitochondrial respiration and upregulation of metabolic pathways linked to proliferation and tumorigenicity. Functionally, uptake of astrocyte mitochondria promotes cell cycle progression to proliferative G2/M phases and enhances self-renewal and tumorigenicity of GBM. Collectively, our findings reveal a host–tumor interaction that drives proliferation and self-renewal of cancer cells, providing opportunities for therapeutic development.

Mitochondria are vital in cell metabolism through their role in generating ATP via oxidative phosphorylation; yet, they have also been implicated in numerous other cellular functions, including apoptotic cell death, inflammation, stem cell differentiation and autophagy[1,2]. After the discovery of the Warburg effect identifying conversion of glucose to lactate in the presence of oxygen to fuel cancer growth[3], aerobic glycolysis has been assumed to be the main energy pathway for cancer cells[4], including in glioblastoma (GBM)[5], the most common primary adult brain tumor. However, recent reports suggest a more complex situation where mitochondrial respiration is also an alternative energy source[6,7]. The existence of multiple metabolic phenotypes is in line with the cellular heterogeneity of this disease[8–10].

While this heterogeneity may arise from variation in cell-intrinsic metabolic regulation, it may also arise via interaction with the tumor microenvironment (TME), namely by transfer of metabolic signals, including mitochondria themselves, from the TME to tumor cells. In many contexts, dynamic microenvironmental interactions have been shown to be major drivers of tumor growth and therapeutic resistance in GBM[11–13], while the underlying direct cell–cell communication mechanisms remain poorly understood.

Transfer of mitochondria has been demonstrated between different cell types and via different routes. Mitochondria transfer by extracellular vesicles from astrocytes to neurons after stroke has been documented in vitro and in vivo[14], identifying a CD38/cADP-dependent mechanism using calcium signaling. Extracellular vesicles as a mode of mitochondria transfer has also been shown for mesenchymal stem cells[15], indicating that transfer by secretion is a viable route for this organelle. In other studies, mitochondria transfer mechanisms independent of secreted particles have been proposed[16–18]. Intercellular membrane protrusions known as tunneling nanotubes have been

e-mail: hrvoje.miletic@uib.no; lathiaj@ccf.org

implicated in organelle transport[19] and more recently in mitochondria transfer[16–18]. By connecting cells over distances that may exceed 100 µm (refs. 20,21), tunneling nanotubes are prime avenues for intercellular cross-talk[22]; composed of components like actin and microtubules[22], they maintain a close cytoskeletal relationship[22].

Tumor microtubes (MTs) are similar structures; however, they are thicker and more stable than tunneling nanotubes and can reach lengths of more than 500 µm in vivo[23]. MTs have so far only been described in glioma, particularly in GBM, and have been identified as an important mode of intercellular communication, invasion and therapy resistance[24–27]. Growth-associated protein 43 (GAP43), a neuronal protein known for its important role in axon guidance[28], is a major structural protein of MTs. Knockdown of GAP43 in GBM cells reduced MT formation and tumorigenicity in vivo[24]. This work highlighted the relevance of the interconnected network of GBM cells formed by GAP43$^+$ MTs for tumor growth. In a recent study, mitochondria were reported to be exchanged in vitro among GBM cells interconnected via MTs[29].

Given the reports of horizontal mitochondria transfer in the brain across distinct cell types under pathologic conditions[14], we hypothesized that GBM also acquires functional mitochondria from non-malignant cells in the TME, comprising an unexplored layer of metabolic heterogeneity. Here, we show that GBM cells acquire host mitochondria from astrocytes through a contact-dependent mechanism facilitated by GAP43$^+$ structures consistent with MTs, resulting in enhanced metabolic activity and augmented tumorigenicity. Our findings identify mitochondria transfer from the TME as a fundamental protumorigenic mechanism in GBM.

Results

GBM acquires mitochondria from the microenvironment

To assess whether non-malignant host cells could transfer mitochondria to GBM in vivo, we orthotopically implanted green fluorescent protein (GFP)-expressing syngeneic mouse GBM models (SB28 and GL261) into transgenic C57BL/6 mice expressing a mitochondria-localized mKate2 fluorophore fused to the localization peptide of cytochrome *c* oxidase 8 (mito::mKate2 mice[30]; Fig. 1a). Confocal microscopy of GBM tumors from mito::mKate2 mice revealed mKate2$^+$ puncta within 15–60% of GFP$^+$ GBM cells (Fig. 1b–f and Extended Data Fig. 1), demonstrating that host cell mitochondria were acquired in vivo by orthotopic GBM tumor cells. By co-staining tissue sections with wheat germ agglutinin (WGA) to highlight glycoprotein-rich structures[31], we observed host mKate2$^+$ mitochondria in transit at host–tumor interfaces along intercellular connections between GFP$^+$ GBM cells and GFP$^-$ host cells (Extended Data Fig. 1). To determine whether mitochondria transfer occurred in the context of human GBM in vivo, we first injected a high-titer mitoDsRed lentivirus into the brain of nude rats to transduce normal brain cells with a mitochondria fluorescent tag. After 7 d, P3 GFP$^+$ human-derived GBM stem-like cells (GSCs) were injected in the same location (Fig. 1g). High-resolution confocal images verified mitochondria transfer from stromal cells to tumor cells, supporting our mouse in vivo data (Fig. 1g). When reconstructed in three dimensions, the mitoDsRed signal was present within acceptor cells positive for GFP. We verified these results in a second human-derived GSC line GG16 transduced with mito-GFP and by immunostaining with a human-specific nestin antibody (Extended Data Fig. 2).

Having observed mitochondria transfer from the TME to mouse and human GBM models, we proceeded to interrogate the identity of the host mitochondria donor cells. GBM tumors in mouse models and humans are known to have substantial infiltration by both brain-resident glia and peripheral immune cells that transmigrate into the TME[13]. We established orthotopic GBM tumors in wild-type C57BL/6 mice that had first received lethal irradiation with subsequent bone marrow reconstitution from mito::mKate2 mice (mito::mKate2→WT) to restrict mito::mKate2 expression to bone marrow-derived immune cells (Extended Data Fig. 3a). Analysis of single-cell suspensions by flow cytometry indicated negligible host mitochondria transfer to GFP$^+$ GBM cells in mito::mKate2→WT mice, while 20–60% of GFP$^+$ GBM cells were mKate2$^+$ in mito::mKate2 mice (Extended Data Fig. 3b,c). Taken together, these data suggest that brain-resident cells, not tumor-infiltrating immune cells, were the major donors of mitochondria to GBM cells in vivo.

To further elucidate the identity of the predominant mitochondria donor cell populations, we cocultured prevalent tumor-infiltrating cell types with GFP$^+$ GBM cells at a 1:2 donor:recipient ratio. After 2 h, we assessed the percentage of mKate2$^+$ cells as a marker of mitochondria transfer (schematized in Fig. 2a). Consistent with our in vivo observations, we found that brain-resident glia (astrocytes and microglia) donated significantly more mitochondria on a per-cell basis than bone marrow-derived macrophages, with astrocytes having higher transfer rates (Fig. 2b and Extended Data Fig. 4a). While further polarization of macrophages to an M2- or M1-like phenotype potentially favored increased mitochondria transfer, the degree of transfer was, on average, five- to tenfold less than that observed with the brain-resident glia in vitro (Extended Data Fig. 4b).

Given our observation that astrocytes displayed high rates of mitochondria transfer to mouse models of GBM and their previously described interconnected nature with GBM in vivo[32], we focused our subsequent studies on this glial cell population. We began by coculturing either mito-mCherry or mitoDsRed immortalized human astrocytes with six different human-derived GSCs (L1, DI318, 3832, GG16, P3 and BG5) for 3–4 d to interrogate the applicability of our findings in human models of disease. As with mouse GBM models, we found that human-derived GSCs acquired mitochondria from astrocytes, with flow cytometry revealing a transfer rate of 5–40% (Fig. 2c,d and Extended Data Fig. 4c). We confirmed the internalization of astrocyte mitochondria by confocal microscopy of the GSCs, whereby the fluorescent protein-tagged mitochondria were visualized entirely within GSCs with cytoplasm prelabeled with CellTrace dye or expressing GFP (Extended Data Fig. 4d,e). We confirmed that astrocyte-to-human GBM transfer of mitochondria was relevant in vivo using the human orthotopic GBM model (P3) derived from Fig. 1g. We identified mitoDsRed$^+$ astrocytes (glial fibrillary acidic protein (GFAP$^+$) and GFP$^-$) surrounding GFP$^+$ GBM cells with transferred mitoDsRed$^+$ mitochondria (Fig. 2e and Extended Data Fig. 4f). ImageStream analysis on a distinct set

Fig. 1 | GBM cells acquire host mitochondria from the TME. a, GFP-expressing GL261 and SB28 cells were implanted intracranially into wild-type (WT) and mito::mKate2 (mK) mice, and tumors were analyzed at humane endpoint. **b**–**e**, Single focal planes (*xy*) and *z*-stack orthogonal reconstructions (*xz*, *yz*) at areas of SB28 (**b**,**c**) and GL261 (**d**,**e**) tumor–host cell interfaces. Yellow arrowheads indicate host mKate2$^+$ mitochondria (Mito) within recipient tumor cells. Cyan arrowheads indicate WGA-labeled tether-like structures connecting tumor and host cells. **f**, Three-dimensional confocal imaging segmentation-based estimation of mKate2$^+$GFP$^+$ GBM cell frequency from two to three visual fields from $n = 3$ (SB28) and $n = 2$ (GL261) WT and $n = 3$ (SB28) and $n = 4$ (GL261) mK mice; $^{***}P = 0.0003$ (SB28) and $P < 0.0001$ (GL261). Data were analyzed by two-tailed *t*-test. See also Extended Data Fig. 1 for additional data, including technical controls. **g**, Mitochondria transfer between the TME (mitoDsRed$^+$) and human GBM cells (GFP$^+$) in vivo. MitoDsRed lentivirus was injected into the brains of nude rats. Seven days later, human P3 GFP$^+$ GSCs were injected into the same area. Confocal microscopy images of P3 GFP$^+$ xenograft tumors are representative of at least six ×100 images across three biologically independent animals. Details of the area along the tumor surface are shown in (i), with colocalization of GFP$^+$ and mitoDsRed$^+$ signal in (ii) and (iii). A 3D reconstruction of the mitoDsRed$^+$ mitochondria (white arrows) seen from above, without (iv) and with (v) the GFP$^+$ cell borders, is shown. From below, the mitoDsRed$^+$ mitochondria are also visible in (vi) and reside within the cell in (vii). ii, ×1.5 magnification; iii–vii, ×3 magnification.

https://doi.org/10.1038/s43018-023-00556-5

of human-derived co-culture models, where donor astrocytes were tagged with mito-GFP and GBM recipients with red-fluorescent protein (RFP), revealed similar results with internalized donor mitochondria in recipient cells (Extended Data Fig. 4g–i). Finally, we confirmed that transferred mitochondria labeled with mito-mCherry expressed the mitochondrial protein translocator of outer mitochondrial membrane 20 (TOMM20) by colocalization analysis, and the protein was distributed within the mitochondrial network of the receiving GBM cell (Extended Data Fig. 5 and Supplementary Video 1 and 2). In summary, we observed mitochondria transfer from the TME to GBM in vivo and in vitro and identified astrocytes as a major mitochondria donor.

GAP43$^+$ MTs facilitate mitochondria transfer

We considered that mitochondria transfer could occur via secretion[14] and/or cell contact[24,33]. To discriminate between the two mechanisms, we compared the mitochondria transfer rate of co-cultures to that of

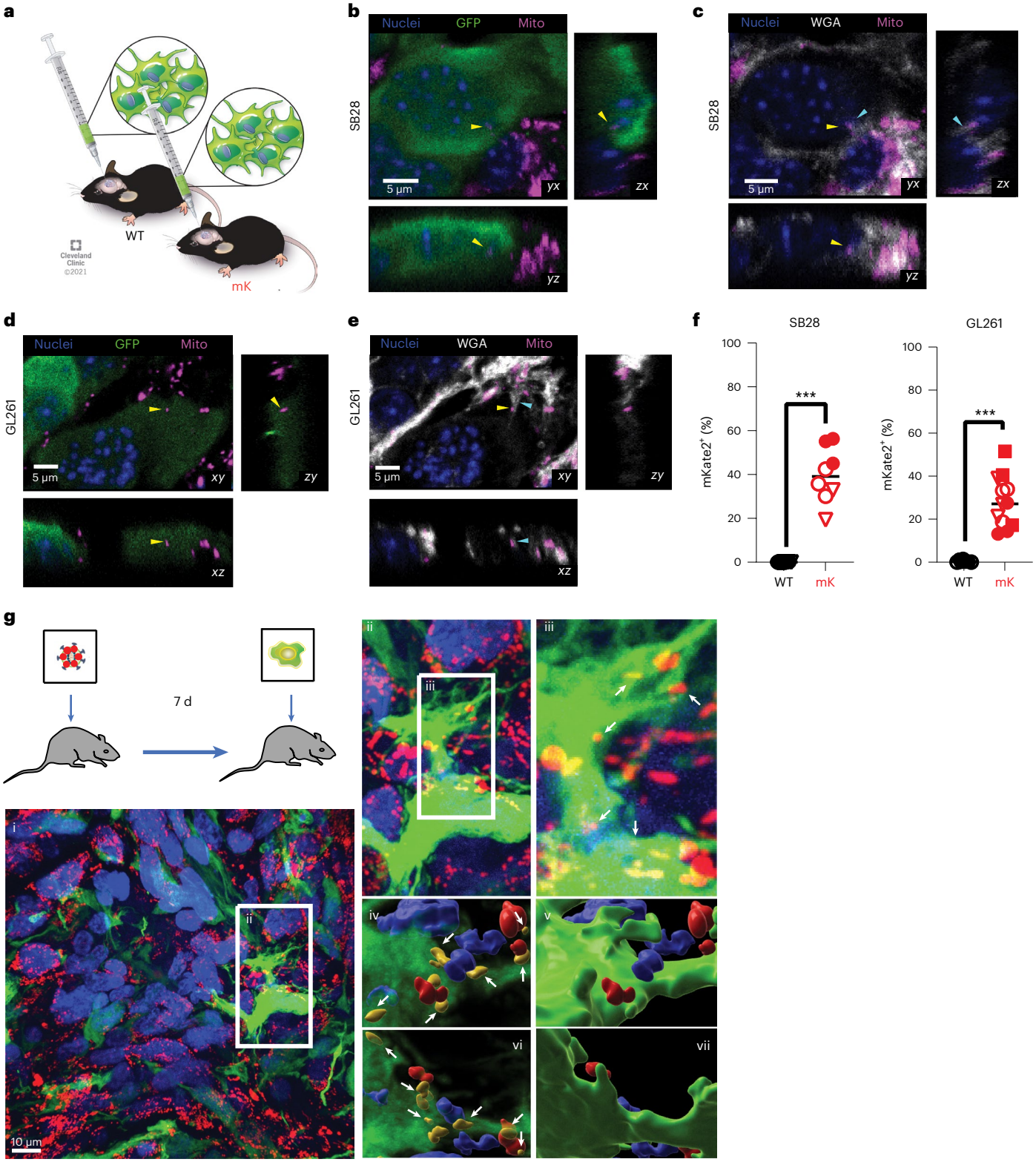

https://doi.org/10.1038/s43018-023-00556-5

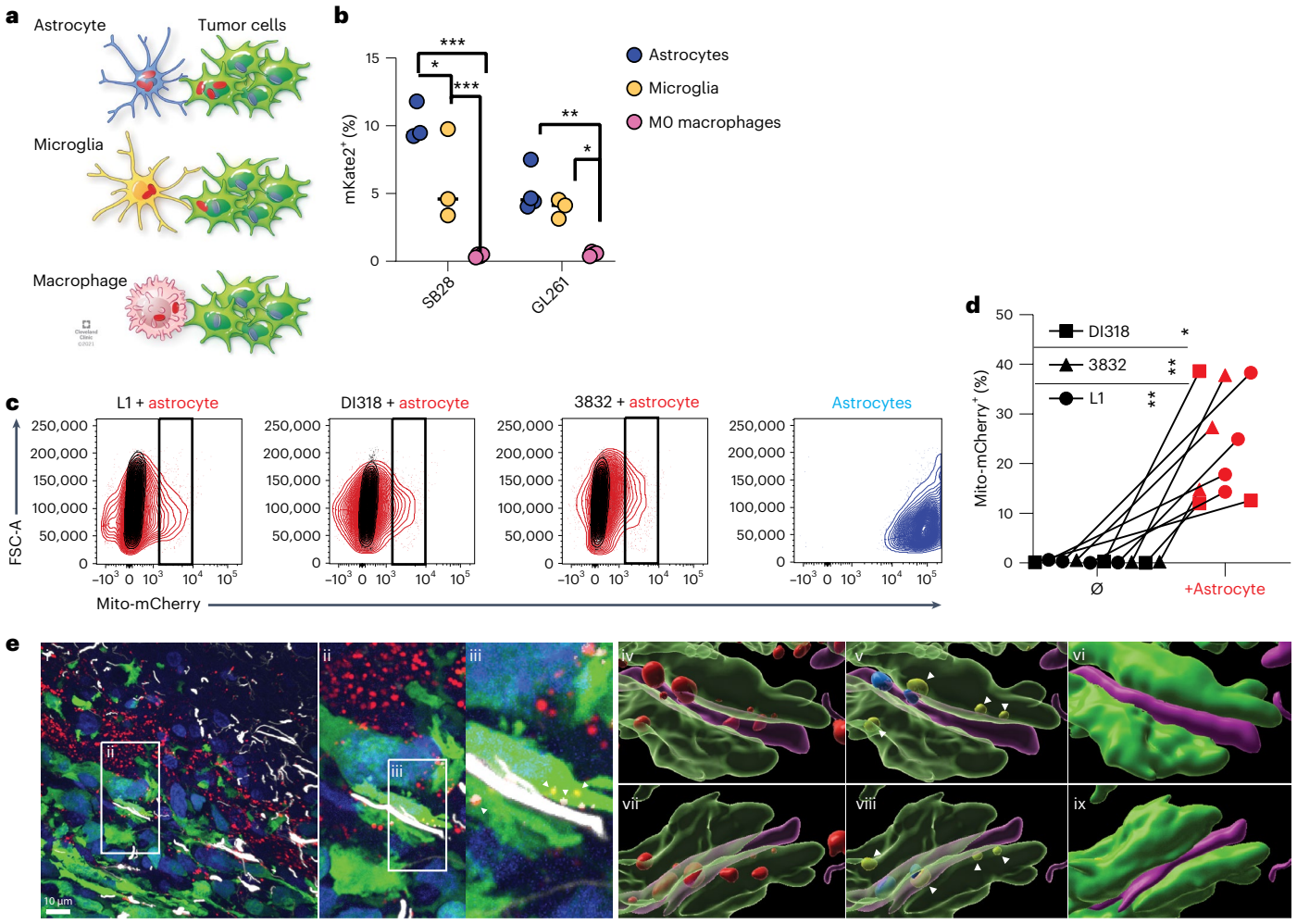

Fig. 2 | GBM cells acquire mitochondria from astrocytes. a, GBM cells were cocultured with astrocytes, microglia or macrophages from mK mice for 2 h, and mitochondria transfer was analyzed by flow cytometry. **b**, Relative frequency of mKate2$^+$GFP$^+$ GBM cells in co-cultures; $n = 3$ (SB28) and 4 (GL261) independent experiments; $^*P < 0.05$, $^{**}P < 0.01$, $^{***}P < 0.001$. Data were analyzed by two-way analysis of variance (ANOVA). **c**,**d**, Human-derived GSCs were cocultured with immortalized mito-mCherry$^+$ human astrocytes for 4 d. Mito-mCherry$^+$ GSCs (black rectangle gate) were quantified by flow cytometry (**c**), as summarized in **d**; $n = 3$ (3832), 3 (DI318) and 4 (L1) independent experiments. Data were analyzed by two-way ANOVA; $P = 0.006$ (L1), 0.03 (DI318) and 0.007 (3832). **e**, Mitochondria transfer between astrocytes (mitoDsRed$^+$ and GFAP$^+$) and human GBM cells (GFP$^+$) in vivo. Confocal microscopy of a GFP$^+$ P3 xenograft tumor immunostained with antibodies to GFAP (white color) was used to visualize astrocytes. Images are representative of at least six ×100 images across three biologically independent animals. Mitochondria transfer is highlighted in an invasive tumor area with colocalization of GFP$^+$ and mitoDsRed$^+$ signal in (i). Images in (ii) and (iii)–(ix) represent ×1.5 and ×3 magnifications, respectively. A 3D reconstruction of the mitoDsRed$^+$ mitochondrial signal both within and around the GFP$^+$ and GFAP$^+$ surfaces is shown in (iv). The mitoDsRed$^+$ mitochondria colocalized within the GFP$^+$ tumor cell borders (yellow) and within the purple reconstructed GFAP$^+$ astrocytic processes (blue), seen from above without (v) and with (vi) GFP$^+$ and GFAP$^+$ cell borders. From below, mitoDsRed$^+$ mitochondria are also visible in (vii) and reside within the GFP$^+$ and GFAP$^+$ regions in (viii) and (ix).

transferred donor-conditioned medium (mouse models; Extended Data Fig. 6a,b) or cells separated by a 5-µm porous transwell insert (human models; Fig. 3a). Regardless of the separation method, transfer primarily occurred when donor and recipient cells were in physical contact, and there was only low-level transfer by secretion that was near the limit of detection of our assays. Live confocal microscopy of mitochondria transfer from astrocytes to mouse GBM cells was also visualized in adjacent cells (Extended Data Fig. 6c and Supplementary Video 3). Transfer was abrogated in both mouse and human models when co-cultures were incubated at 4 °C (Extended Data Fig. 6d,e), suggesting that this was an active, energy-dependent process rather than a passive event. Taken together, these results indicate that active physical interaction of tumor and donor cells is required for effective mitochondria transfer, in line with imaging of in vivo brain tumor models (Figs. 1 and 2 and Extended Data Figs. 1 and 2).

MTs are established conduits of intercellular communication and network formation in GBM and, thus, are also potential mediators of mitochondria transfer[24,32,34–36]. To visualize mitochondria within the interfaces of GBM cells, we performed confocal microscopy of co-cultures immunostained for TOMM20 and actin. In addition to a perinuclear localization, mitochondria were found in MT connections between tumor cells (P3 model; Fig. 3b), consistent with a previous study reporting that mitochondrial components localize in between astrocyte and GBM cell connections in vitro[37]. Their intratubular location was confirmed by *z* stack. Importantly, confocal microscopy of mitoDsRed$^+$ astrocytes and GFP$^+$ P3 co-cultures immunostained with actin showed MTs with mitoDsRed$^+$ mitochondria connecting both cell types. These were present in the vicinity of transferred mitochondria (Fig. 3c). We also found astrocytic mitoDsRed$^+$ donor mitochondria shuttling between connected tumor acceptor cells, indicating that

https://doi.org/10.1038/s43018-023-00556-5

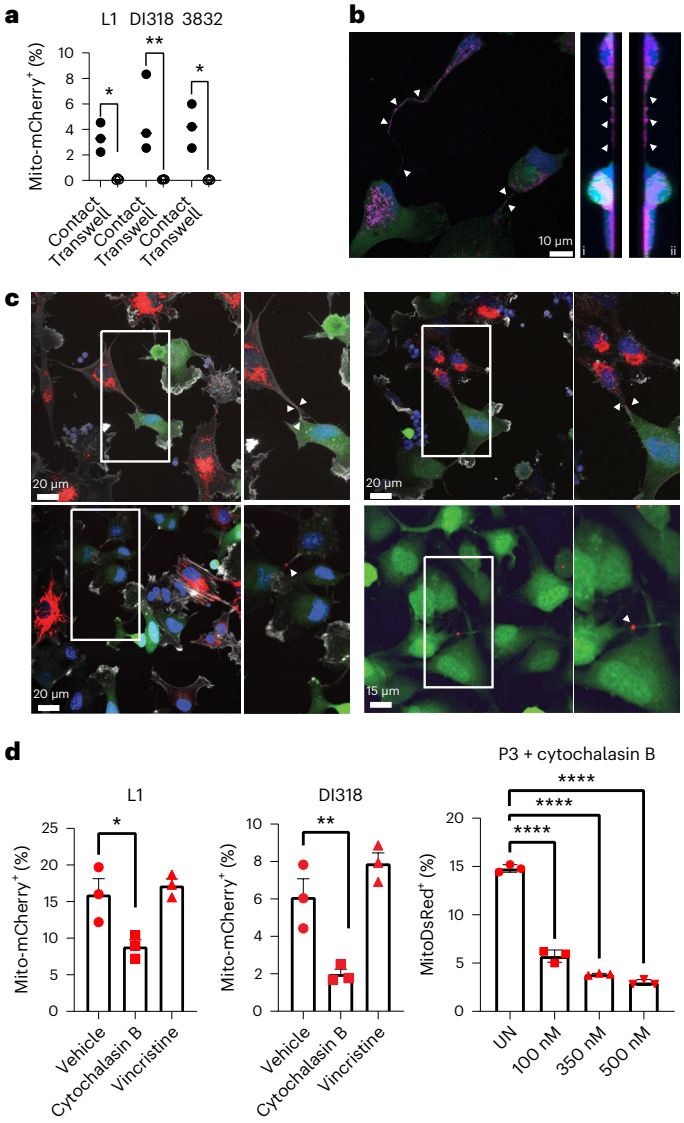

Fig. 3 | Astrocytes transfer mitochondria to GBM via actin-based intercellular connections. a, Human-derived GSCs (L1, DI318 and 3832; bottom) and astrocytes (top) were separated from each other with 5-μm porous transwell inserts. Twenty-four hours later, mitochondria transfer was analyzed based on mito-mCherry signal; $n = 3$ independent experiments; $P = 0.02$ (L1), 0.007 (DI318) and 0.01 (3832). Data were analyzed by two-way ANOVA. **b**, Presence of mitochondria within MTs connecting P3 GFP$^+$ cells. Immunostaining with TOMM20, representative of at least eight ×100 images across three biologically independent co-cultures, is shown. Intratubular location is confirmed by *z* stacking, seen from the left in (i) and the right in (ii) side. Arrows indicate TOMM20$^+$ signal. **c**, Co-culture between mitoDsRed$^+$ astrocytes and GFP$^+$ P3 cells immunostained with F-actin (white) to visualize membrane extensions connecting the two cell types, emphasized with high magnification. Images are representative of at least 20 ×60 images across three biologically independent co-cultures. Arrows indicate mitoDsRed$^+$ mitochondria in intercellular connections and transferred mitoDsRed$^+$ mitochondria. MitoDsRed$^+$ mitochondria are also observed in MT connections between two tumor cells, confirming the exchange of mitochondria within the whole network of tumor–tumor/tumor–astrocyte connections. Insets: ×1.5 magnification. **d**, Human-derived GSCs were cocultured for 24 h with immortalized mito-mCherry$^+$ and mitoDsRed$^+$ human astrocytes in the presence of actin (cytochalasin B) or microtubule (vincristine) polymerization inhibitors or vehicle control (UN). The frequency of mito-mCherry$^+$ or mitoDsRed$^+$ GSCs was assessed by flow cytometry; $n = 3$ independent experiments. Data are presented as mean ± s.e.m. (L1 and DI318) and mean ± s.d. (P3); $^*P = 0.03$ (L1), $^{**}P = 0.01$ (DI318), $^{***}P < 0.0001$ (P3). Data were analyzed by one-way ANOVA with Holm–Sidak multiple comparison correction.

astrocytic mitochondria can be further exchanged within the complete network of tumor–tumor connections (Fig. 3c). After visualizing mitochondria in transit along intercellular connections containing actin filaments, we hypothesized that the actin cytoskeleton was critical in facilitating mitochondria transfer. Indeed, inhibition of actin polymerization by cytochalasin B resulted in a significant decrease in transfer rate, without an effect on cell viability (Fig. 3d and Extended Data Fig. 6f–h). By contrast, inhibition of tubulin polymerization with vincristine had no effect on mitochondria transfer (Fig. 3d).

Previous work showed that GAP43 facilitated the formation of an interconnected network of GBM cells in vivo, which enabled connexin 43-mediated propagation of calcium waves[24]. GAP43 is an actin-associated protein that facilitates neurite outgrowth via growth cones[38,39]. We visualized that GAP43 also localized to the cellular projections of GBM cells and astrocytes in co-culture (Fig. 4a). When we knocked down the expression of GAP43 in human-derived GSCs, we observed a decrease in the number of cellular projections (Fig. 4b,c and Extended Data Fig. 6i), as previously reported[24,34]. Importantly, we found that mitochondria transfer from astrocytes was significantly decreased when GAP43 was knocked down in GSCs alone or in both GSCs and astrocytes (Fig. 4d,e and Extended Data Fig. 6i,j). These data identify a role for GAP43 in facilitating mitochondria transfer from astrocytes to GBM.

Astrocyte mitochondria metabolically reprogram GBM cells

We hypothesized that receiving entire organelles from astrocytes would have biologically important downstream functional sequelae in recipient GBM cells. We first interrogated how mitochondria transfer affected cells transcriptionally by bulk RNA sequencing (RNA-seq) of sorted mouse GBM cells with (mKate2$^+$) or without (mKate2$^-$) astrocyte mitochondria acquisition from co-cultures (Extended Data Fig. 7a). Unsupervised clustering of RNA-seq data revealed that tumor cells had a distinct gene expression profile compared to astrocytes, confirming that sorted mKate2$^+$ SB28 cells were not meaningfully contaminated by astrocytes from the co-culture (Extended Data Fig. 7b–d). Genes that were upregulated >1.5-fold in mKate2$^+$ tumor cells compared to mKate2$^-$ tumor cells (Extended Data Fig. 7e,f and Supplementary Table 1) were enriched within pathways related to mitochondrial biology, in particular electron transport and mitochondrial organization (Extended Data Fig. 7a).

Given the central role of mitochondria in ATP production and the results of our RNA-seq analysis, we investigated whether an increase in functional mitochondria through transfer causes a measurable change in metabolic parameters, in particular oxygen consumption rate. We performed a mitochondrial stress test on GFP$^+$ acceptor cells (P3 model) with high and low mitochondria transfer from mitoDsRed$^+$ astrocytes compared to control cells from the same co-cultures using the Seahorse system. After measuring the basal respiration rate, we sequentially added electron transport chain inhibitors to evaluate the changes in maximal respiration capacity. Interestingly, both basal respiration and maximal respiration rate were increased in accordance with mitochondria transfer (Fig. 5a–c). When dividing the cells into metabolic subgroups based on basal respiratory and glycolytic rates, cells with the highest mitochondria transfer were more aerobic and energetic than cells with lower transfer and controls (Fig. 5d). We further characterized the metabolic profile of a panel of GSCs after co-culture with human astrocytes by adapting a previously reported metabolic flow cytometry panel[40]. The mitochondrial ATP synthase subunit ATP5A was among the most consistently upregulated metabolic proteins in recipient GSCs (Fig. 5e and Extended Data Fig. 8a) and in mouse models of GBM (Extended Data Fig. 8b,c). We evaluated whether these cells with higher respiratory capacity and ATP synthase levels generated more ATP. Across multiple human-derived GBM models, we verified that GBM cells that acquired mitochondria from astrocytes also had higher levels of ATP as measured by luminescence reporter assay (Fig. 5f,g).

https://doi.org/10.1038/s43018-023-00556-5

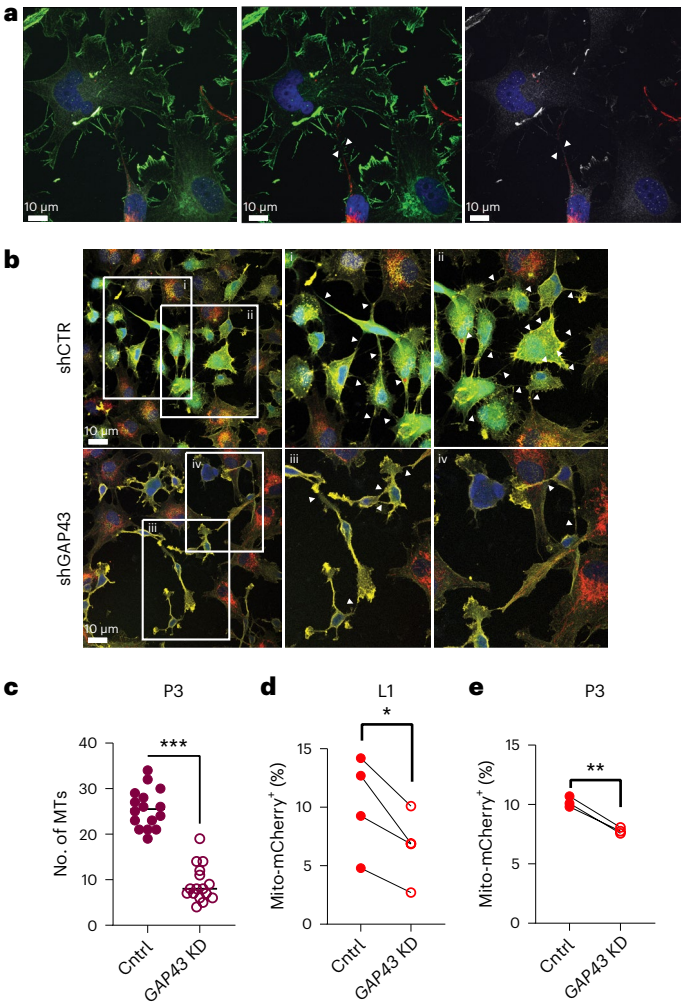

Fig. 4 | GAP43 facilitates mitochondria transfer via tumor–astrocyte MTs. **a**, Presence of GAP43$^+$ MT-like connections (arrows) between mitoDsRed$^+$ astrocytes and P3 tumor cells. Immunostaining for GAP43 (white) and actin (green) is shown. Left: mitoDsRed (red), GAP43 and actin. Middle: mitoDsRed and actin. Right: mitoDsRed and GAP43. Images are representative of at least four ×100 images across three biologically independent co-cultures. **b**, Co-culture of mitoDsRed$^+$ astrocytes and GFP$^+$ P3 short hairpin GAP43 (shGAP43) cells indicates fewer membrane connections between donor and recipient cells than observed in GFP$^+$ P3 short hairpin control (shCTR) cells. Immunofluorescence staining with F-actin (yellow) is shown and is further visualized at increased magnification (i–iv). Arrows indicate MTs. Insets: 2 × magnification. **c**, Quantification of MTs from **b** across 16 independent ×60 images across $n = 4$ independent co-culture experiments per group. Data are shown as the mean ± s.d.; ***$P < 0.0001$. Data were analyzed by two-tailed *t*-test; Cntrl, wild type; KD, knockdown. **d**, Wild-type or *GAP43*-knockdown L1 human-derived GSCs were cocultured for 24 h with matching wild-type or *GAP43*-knockdown mito-mCherry$^+$ astrocytes. Astrocyte-derived mitochondria transfer to GSCs was quantified by flow cytometry; $n = 4$ independent experiments; *$P = 0.01$. Data were analyzed by two-tailed *t*-test. **e**, Wild-type or *GAP43*-knockdown P3 human-derived GSCs were cocultured for 24 h with mitoDsRed human astrocytes. Astrocyte-derived mitochondria transfer to GSCs was quantified by flow cytometry; $n = 3$ independent experiments; **$P = 0.001$. Data were analyzed by two-tailed *t*-test.

Collectively, these data show that transferred astrocyte mitochondria are bioactive and lead to augmented mitochondrial respiration and ATP production in recipient GBM cells.

Mitochondria can further influence cellular biology by modulating diverse metabolic pathways[41], and there is increasing evidence that they influence intracellular phosphorylation signaling cascades[42,43]. We thus performed a metabolite mass spectrometry assay and 584-site protein phosphorylation array on sorted GBM cells from co-cultures with astrocytes to interrogate the functional consequence of mitochondria uptake. Metabolite enrichment analysis revealed multiple upregulated metabolic pathways in mKate2$^+$ GBM cells shared between both GL261 and SB28 mouse models (Fig. 6a, Extended Data Fig. 8d and Supplementary Table 2). Among these pathways was amino acid and nucleotide metabolism, previously linked to proliferation, self-renewal and tumorigenicity in GBM[44–46]. Metabolomic analysis of the sorted human-derived L1 cells showed that mCherry$^+$ cells have higher amounts of glutamate, α-ketoglutarate, glutathione and essential amino acids than mCherry$^-$ cells (Fig. 6b and Extended Data Fig. 8e,f). Glutamate is one of three amino acids in glutathione, a major cellular antioxidant, and glutamate metabolism is a principal route for assimilation of nitrogen in de novo nucleotide synthesis, which promotes numerous oncogenic processes in gliomas[47,48]. This suggests that transfer of mitochondria may be helping the GBM cells support proliferation and protect against oxidative stress. Our phosphoprotein array also revealed changes in the phosphorylation levels of numerous signaling and effector proteins in human-derived GSCs that received astrocyte mitochondria, many of which mapped to proliferation and cell cycle pathways (Fig. 6c and Supplementary Table 3). These findings are consistent with metabolic reprogramming of recipient cells beyond increased mitochondrial respiration, along with intracellular signaling with potential effects on cell cycle regulation and other processes.

Mitochondria transfer increases GBM tumorigenicity

To determine whether the metabolic and signaling changes that we observed in GBM cells that acquired astrocyte mitochondria resulted in altered cell cycle regulation, we performed cell cycle analysis in our models of mitochondria transfer by DNA staining and flow cytometry across multiple human-derived GSC models. We observed a consistent increase in the proportion of cells in the proliferative G2/M phases of the cell cycle following acquisition of astrocyte mitochondria (Fig. 7a,b and Extended Data Fig. 9a). This observation was consistent in vivo when analyzing mouse GBM models from orthotopic tumors established in mito::mKate2 mice (Fig. 7c,d). Moreover, orthotopic mouse GBM tumors originating from sorted cells that had acquired astrocyte mitochondria had a higher mitotic index (Extended Data Fig. 9b–e), suggesting that the increased proliferation phenotype was retained in vivo. Previous reports demonstrated that GSCs could take up isolated cell-free mitochondria added to cell culture medium[49]. Addition of astrocyte-derived mitochondria to human-derived GSCs was sufficient to recapitulate the increased proportion of cells in G2/M phases of the cell cycle (Fig. 7e–g). These data suggest that the transfer of astrocyte mitochondria impacts cell cycle regulation in human GBM models.

To further assess the impact of mitochondria acquisition on self-renewal, we performed limiting dilution sphere formation assays using sorted GBM cells with and without astrocyte mitochondria. In both human and mouse GBM models, we found that cells that acquired astrocyte mitochondria had significantly higher self-renewal capacity, represented as a higher estimated stem cell frequency (Fig. 7h and Extended Data Fig. 10a). While human-derived GSC models expressed high levels of the pluripotency transcription factor SOX2, we found that GSCs that acquired astrocyte mitochondria further upregulated another self-renewal transcription factor, OCT4 (Extended Data Fig. 10b). These findings suggest that mitochondria transfer from astrocytes consists of a previously undescribed TME interaction that promotes GBM self-renewal.

Increased proliferative capacity and self-renewal are central hallmarks of cancer; we thus hypothesized that mitochondria transfer from astrocytes promotes tumorigenicity of GBM. We tested this hypothesis by assessing the lethality (time to death or humane endpoint) and tumor initiation capacity of human-derived GBM cells with and without acquisition of human astrocyte mitochondria by orthotopic implantation in immunocompromised mice. These studies revealed

https://doi.org/10.1038/s43018-023-00556-5

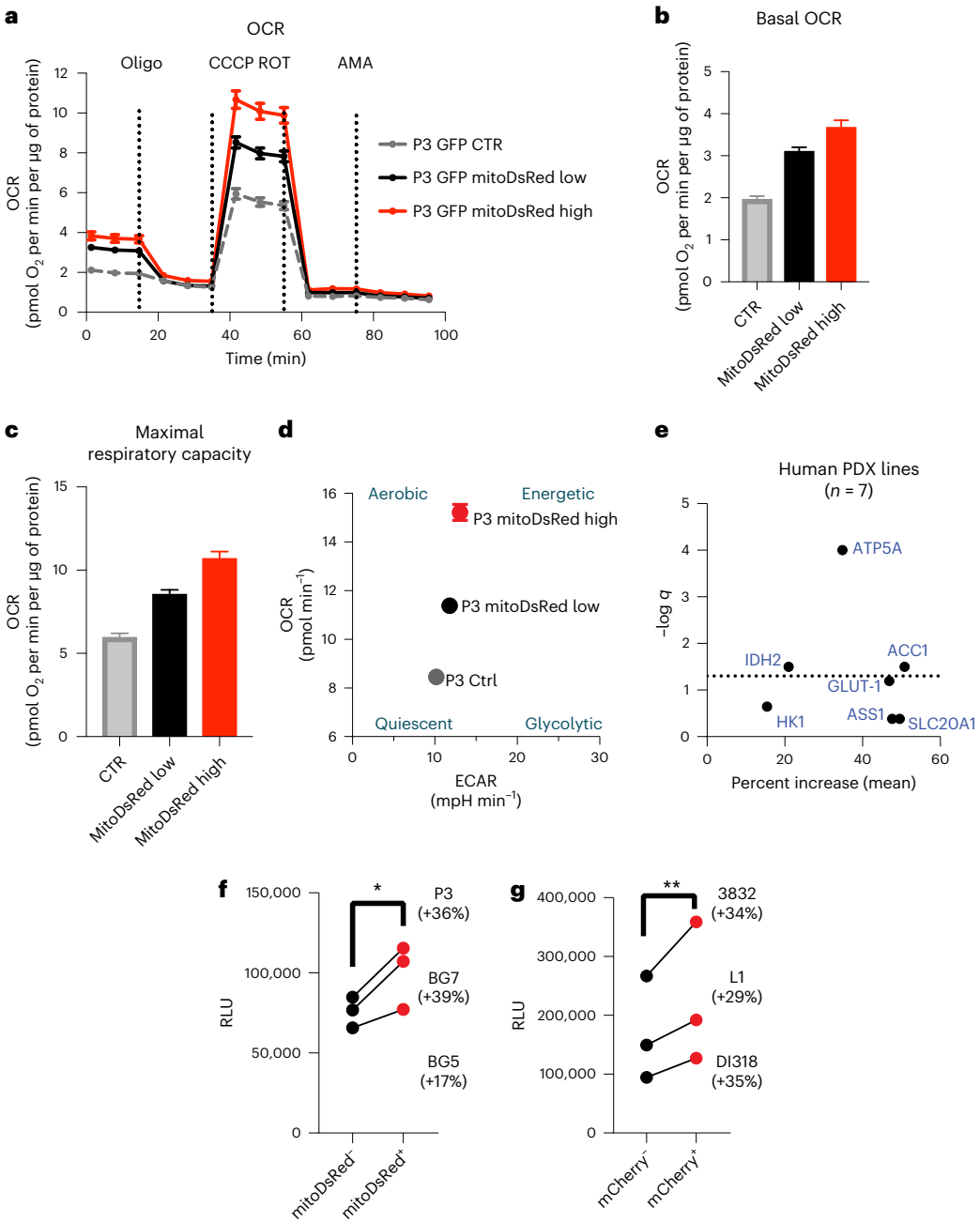

Fig. 5 | Acquisition of astrocyte mitochondria enhances ATP production by mitochondrial respiration in recipient GBM cells. a, Oxygen consumption rate (OCR) was measured in GFP$^+$ P3 cells sorted after transfer with a high or low amount of mitoDsRed$^+$ mitochondria from donor mitoDsRed$^+$ astrocytes and was compared with that in sorted GFP$^+$mitoDsRed$^-$ P3 cells from the same co-culture. Following readings of basal respiration, the stepwise addition of 3 mM oligomycin (Oligo) to measure leak respiration, 1.5 mM CCCP to quantify maximal and reserve capacity and 1 mM rotenone (ROT) followed by 1 mM antimycin A (AMA) to measure non-mitochondrial respiration was performed; CTR, control. **b**, Basal oxygen consumption gradually increased with cumulative mitochondrial content in GFP$^+$ P3 cells. **c**, Maximal respiratory capacity gradually increased with cumulative mitochondria content in GFP$^+$ P3 cells. **d**, Energy map indicating that GFP$^+$ P3 cells with a higher degree of mitochondria transfer from astrocytes have a more aerobic and energetic phenotype than GFP$^+$ P3 cells with less and no mitochondria transfer. Data in **a**–**d** are from a representative experiment from a total of three independent experiments. Data shown as mean ± s.e.m.; $n = 18$ (control), 22 (mitoDsRed low) and 9 (mitoDsRed high) technical replicates; statistical comparison of technical replicates is not shown. ECAR, extracellular acidification rate; mpH, milli pH. **e**, Seven distinct human-derived GSCs were cocultured for 4 d with immortalized mito-mCherry$^+$ human astrocytes and stained with antibodies recognizing key metabolic proteins for downstream flow cytometry quantification. Protein expression was compared between mito-mCherry$^+$ and mito-mCherry$^-$ cells by mixed-effects model analysis. The dotted line represents the statistical significance threshold (false-discovery rate (FDR) < 0.05). **f**, ATP levels in sorted mitoDsRed$^+$ versus mitoDsRed$^-$ cells from distinct human-derived GSCs, measured with the CellTiter-Glo luminescence assay; $n = 3$ independent experiments; $^*P = 0.04$. Data were analyzed by two-tailed ratio paired t-test; RLU, relative light units. **g**, ATP levels in sorted mito-mCherry$^+$ versus mito-mCherry$^-$ cells from three distinct human-derived GSC lines, assessed by CellTiter-Glo luminescence assay; $n = 3$ independent experiments; $^{**}P = 0.003$. Data were analyzed by two-tailed t-test.

https://doi.org/10.1038/s43018-023-00556-5

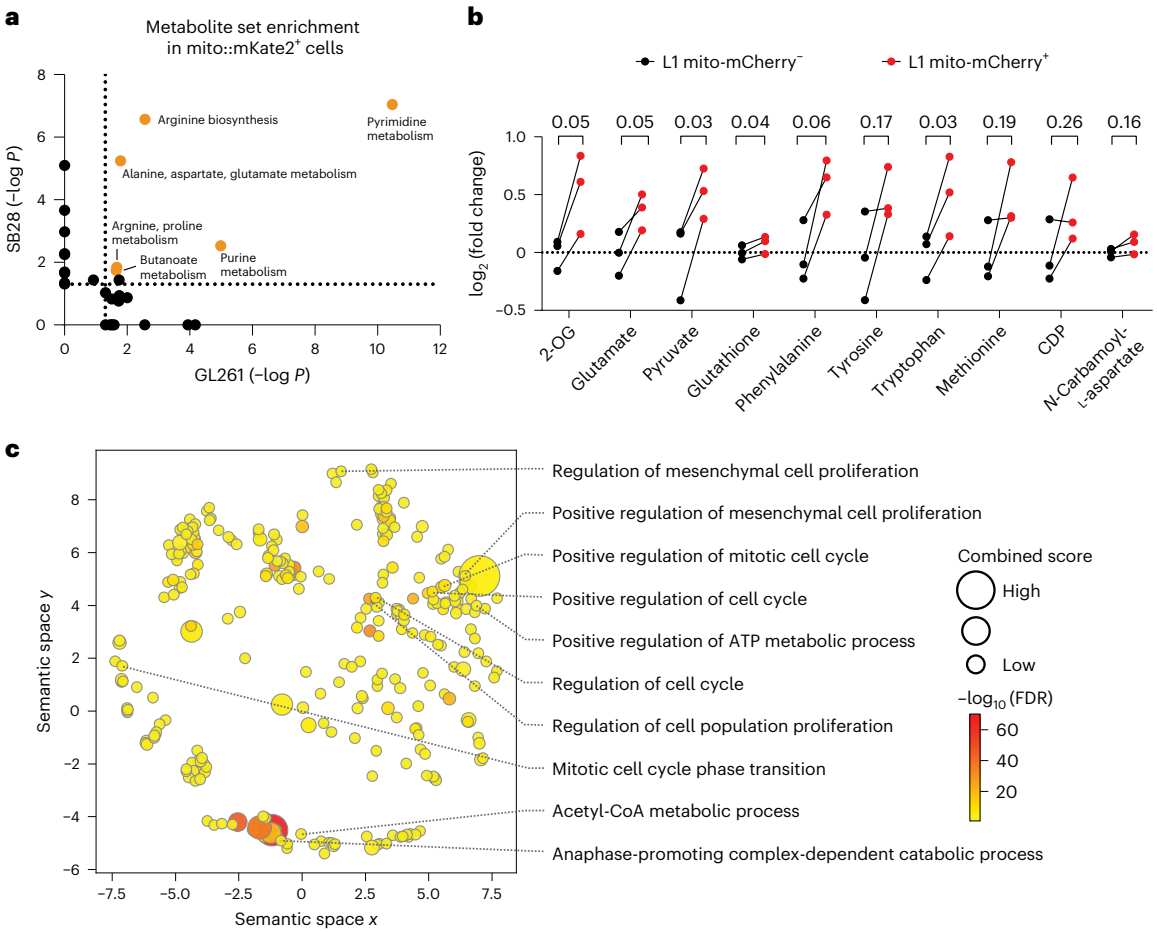

Fig. 6 | Mitochondria transfer from astrocytes reprograms GBM metabolism. **a**, Metabolic pathway analysis (MetaboAnalyst) of metabolites enriched by >20% in mito::mKate2$^+$ versus mito::mKate2$^-$ mouse GBM cells. For each cell model, $n = 3$ independent co-culture experiments were pooled. Dotted lines represent the cutoff for statistical significance ($P < 0.05$). Pathways significantly enriched in both GBM models are highlighted with orange and are labeled with the pathway name. *P* values were calculated with the MetaboAnalyst 5.0 web tool using the one-tailed hypergeometric test for enrichment analysis (expected versus observed metabolites enriched in each pathway). **b**, L1 cells were cocultured with immortalized mito-mCherry$^+$ human astrocytes for 4 d. Relative abundances of metabolites in mito-mCherry$^+$ versus mito-mCherry$^-$ L1 cells indicate higher amino acid and glutathione metabolism in mito-mCherry$^+$ L1 cells; $n = 3$ independent co-culture experiments. Data were analyzed by paired two-tailed *t*-test; 2-OG, α-ketoglutarate; CDP, cytidine-5'-diphosphate. **c**, Phospho-array pathway analysis (Enrichr) of protein phosphorylation sites upregulated in mito-mCherry$^+$ versus mito-mCherry$^-$ L1 cells, depicted with dimensionality reduction in semantic *xy* space. Dots represent significantly upregulated pathways (FDR < 0.05). Selected pathways associated with cell metabolism and proliferation are labeled; $n = 3$ independent co-culture experiments were pooled and analyzed.

that tumors led to symptomatic or lethal disease much faster when originating from GSCs that had acquired mitochondria from astrocytes and had a significantly higher in vivo tumor initiation capacity (Fig. 7i,j and Extended Data Fig. 10c). This observation was similar in mouse GBM models (Extended Data Fig. 10d,e). Thus, beyond altering the phenotype of GBM cells in vitro, mitochondria transfer from astrocytes increases the in vivo tumorigenicity of these cells in animal models.

Discussion

Organelle transfer is an increasingly recognized biological process in models of GBM[35–37] and other cancers[50–52]. Most of the existing knowledge on mitochondria transfer in cancer relies on depicting mitochondrial exchange among tumor cells, in purely in vitro systems, and/or using tumor cells artificially depleted of mitochondria. Thus, the role of mitochondria transfer from the TME to cancer cells (and to GBM in particular) remains poorly understood. Specifically, there is a lack of understanding about the in vivo relevance of mitochondria transfer from the GBM microenvironment, the cell types involved, the mechanism of transfer and its downstream effects on cellular function and tumorigenicity in disease-relevant contexts.

We found that in the context of GBM, mitochondria transfer from the TME is a frequent in vivo event and involves brain-resident glial cell donors. Here, we focused mechanistically on astrocytes as donor cells given their abundance in the brain, and our data identify them as important mitochondrial donors. Our data support that astrocytes in the TME form physical actin-based connections with GBM cells that have strong similarity to the previously described MTs, which are network-forming connections between GBM cells. Our data also support an extension of the previously described interconnected network of GBM to non-malignant astrocytes that has recently been verified by exchange of calcium waves within this network in vivo[24,32]. GAP43, typically found in neuronal projections and critical to GBM growth and the tumor cell network[24], mediates mitochondria transfer from astrocytes in a previously undescribed role for this actin-associated protein.

Our findings further demonstrate that mitochondria transfer from astrocytes to GBM cells drives metabolic reprogramming toward oxidative respiration with increased ATP production. Mitochondria transfer also leads to intracellular signaling via protein phosphorylation linked to cellular proliferation and cell cycle progression.

https://doi.org/10.1038/s43018-023-00556-5

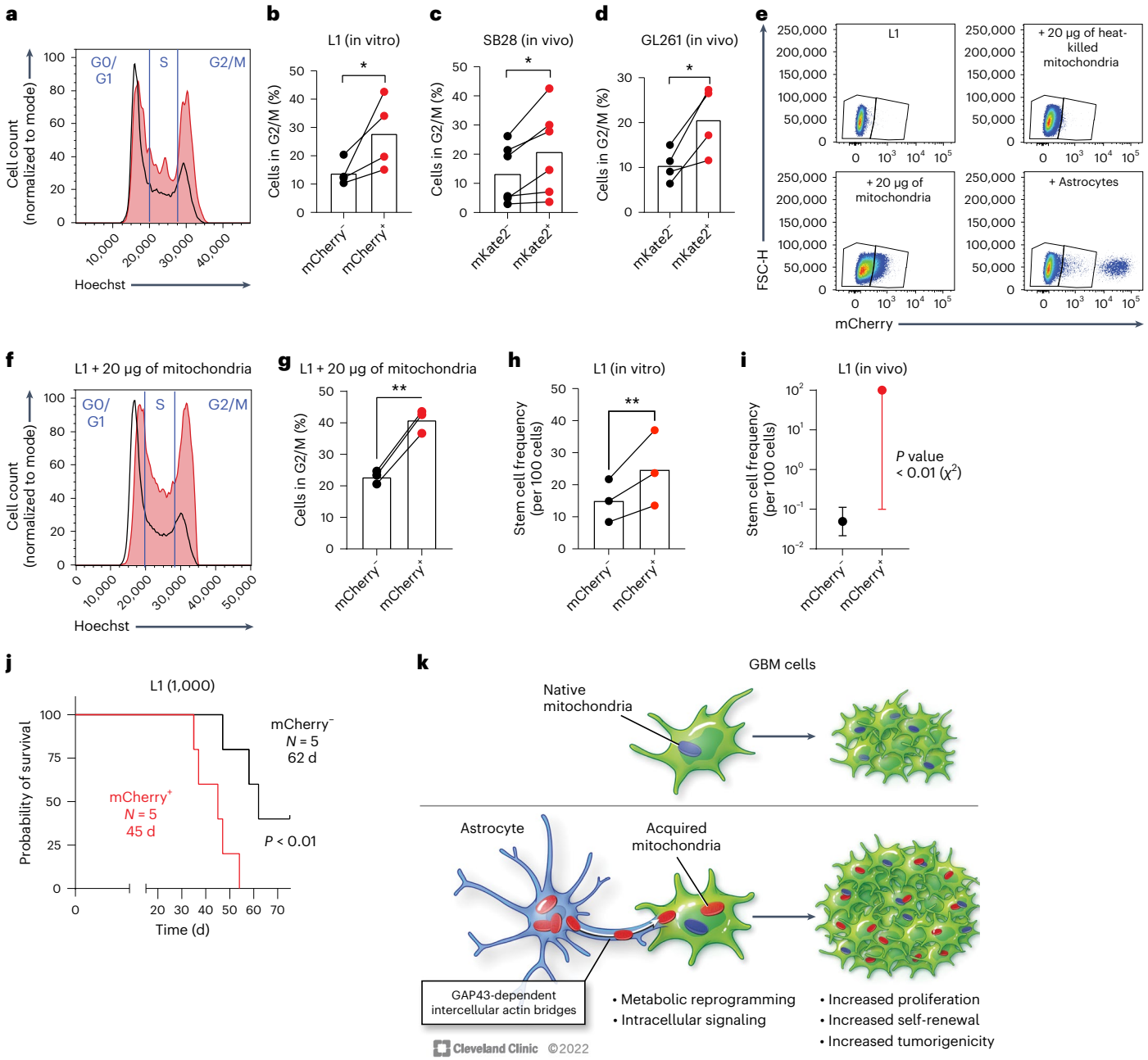

Fig. 7 | Mitochondria transfer from astrocytes drives GBM cell proliferation, self-renewal and tumorigenicity. a,**b**, Human-derived GSCs (L1) were cocultured with immortalized mito-mCherry$^+$ human astrocytes. Representative histograms (**a**) and aggregate data (**b**) of $n = 4$ independent experiments depicting cell cycle analysis by flow cytometric DNA quantification in GSCs that acquired astrocyte mitochondria (mCherry$^+$, red histogram/dots) versus those that did not (mCherry$^-$, black histogram/dots) are shown; $^*P = 0.04$. Data were analyzed by two-tailed *t*-test. **c**,**d**, Cell cycle analysis by ex vivo flow cytometry DNA quantification in GFP-expressing mouse GBM cells obtained from orthotopic tumors in mito::mKate2 mice; $n = 4$–6 mice per tumor model and $N = 6$ (SB28; **c**) and 4 (GL261; **d**) mice per group; $^*P = 0.02$ (SB28) and 0.03 (GL261). Data were analyzed by two-tailed paired *t*-test. **e**–**g**, Cell-free mito-mCherry$^+$ astrocyte mitochondria (intact or heat killed) were added to an L1 culture; vehicle (PBS) or live mito-mCherry$^+$ astrocytes were added to control wells. **e**, Representative dot plots depicting the identification of L1 cells that acquired cell-free mitochondria or mitochondria from cocultured astrocytes. In the +astrocyte condition, the mCherry^{hi} population outside of the gates is composed of the mito-mCherry$^+$ astrocytes. Representative histograms (**f**) and aggregate data (**g**) depicting cell cycle analysis of GSCs that acquired cell-free astrocyte mitochondria (mCherry$^+$, red histogram/dots) versus those that did not (mCherry$^-$, black histogram/dots) are shown; $n = 3$ independent experiments; $^{**}P = 0.003$. Data were analyzed by two-tailed paired *t*-test. **h**,**i**, Estimated stem cell frequency in mCherry$^+$ versus mCherry$^-$ human-derived GBM models sorted from astrocyte co-cultures and subjected to in vitro limiting dilution sphere formation assay (**h**) or in vivo orthotopic tumor initiation assay (**i**); $^{**}P = 0.002$, ratio paired *t*-test, $n = 3$ independent experiments (**h**); $P = 0.005$; compiled data from $n = 15$ NOD *scid* gamma (NSG) mice per group (distributed across three cell-dose levels). Data are shown as mean ± 95% confidence interval; χ^2 test with 1 degree of freedom analyzed by Extreme Limiting Dilution Analysis (ELDA; **i**). **j**, Survival of mice injected orthotopically with 1,000 sorted L1 GSCs per animal; $P = 0.009$. Data were analyzed by log-rank test. Survival analysis of other dose levels is presented in Extended Data Fig. 8. **k**, Schematic overview of findings.

The central finding of our study is that mitochondria transfer from a non-malignant cell of the TME promotes a highly tumorigenic cell phenotype characterized by both increased proliferative capacity and self-renewal (Fig. 7k). This manifested as higher penetrance and faster lethality of orthotopic tumors in vivo. Our findings suggest that the phenotype of increased proliferation and self-renewal driven by acquisition of astrocyte mitochondria before intracranial tumor implantation is sufficient to lead to increased tumorigenicity, while lacking this phenotype at the time of experimental tumor initiation leads to lower GBM cell proliferation. Thus, mitochondria transfer and the shift to oxidative metabolism comprises a fundamental protumorigenic interaction of GBM with its microenvironment. Our study adds a mechanistic understanding to this understudied process, forming the basis of future studies, which could also have broad applicability to tumors outside the central nervous system and other pathological contexts.

Methods

Ethics statements

Human material was obtained from surgeries performed at the Haukeland University Hospital (Bergen, Norway). Written consent was obtained from individuals with procedures that were approved for the projects (project numbers 013.09 and 151825) by the Regional Ethical Committee. Animal experiments were approved by the Institutional Animal Care and Use Committee of Cleveland Clinic and local ethical committee. Animals were treated in accordance with the Norwegian Animal Act.

Human cell culture

The GSC lines P3, GG16 (provided by F. Kruyt, University of Groningen), BG5 and BG7 (ref. 15) were all derived from *IDH* wild-type biopsy specimens from individuals with GBM; 3832 cells were provided by J. Rich (University of Pittsburgh Medical Center) and have been described previously[53]. L1 cells were obtained from B. Reynolds (University of Florida) and have been described previously[54]. DI318 cells were obtained from the Rose Ella Burkhardt Brain Tumor Center biorepository and have been described previously (Cleveland Clinic)[55].

Human-derived GBM cells were cultured in 'complete' Neurobasal medium (NBM): Neurobasal without phenol red (Gibco), supplemented with 2% B-27 supplement (Gibco), 1 mM sodium pyruvate (Gibco), 2 mM L-glutamine (Gibco), 1 U ml^{-1} penicillin + 1 µg ml^{-1} streptomycin (Cleveland Clinic Media Preparation Core), 20 ng ml^{-1} epidermal growth factor (EGF) and 20 ng ml^{-1} fibroblast growth factor 2 (FGF-2; R&D Systems). EGF was not added to P3 cells. Immortalized normal human astrocytes (provided by R. Pieper at University of California, San Francisco, and P. Øyvind Enger at Universitetet i Bergen) were cultured in tissue culture vessels (adherent) in neural stem cell (NSC) medium (DMEM-F12 (Media Preparation Core), 1 U ml^{-1} penicillin + 1 µg ml^{-1} streptomycin, 5% fetal bovine serum (FBS), 1% N2 supplement (Thermo Fisher Scientific), 20 ng ml^{-1} EGF and 20 ng ml^{-1} FGF-2 (R&D Systems)). For experiments involving downstream in vitro limiting dilution assays with L1 and DI318 cell lines, human-derived cells were maintained in DMEM (Cleveland Clinic Media Preparation Core) supplemented with 10% FBS (Thermo Fisher), 1 U ml^{-1} penicillin and 1 µg ml^{-1} streptomycin (Cleveland Clinic Media Preparation Core) for at least 7 d before co-culture with astrocytes.

Human-derived xenograft D456 was provided by D. Bigner (Duke University), and the JX22 cell line was provided by J. Sarkaria (Mayo Clinic). DMEM-F12 containing 10 ng ml^{-1} EGF, 10 ng ml^{-1} FGF, 1% sodium pyruvate, 2% GEM21 (Gemini Bio) and 1 U ml^{-1} penicillin + 1 µg ml^{-1} streptomycin was used to culture the human-derived xenograft lines.

Lentiviral transductions of human cells

Human astrocytes were transduced with mito-mCherry lentivirus (Takara) and selected by fluorescence-activated cell sorting. GAP43 short hairpin RNA (shRNA) and non-target (control) lentiviruses were generated in-house according to the protocol described by Tisconia et al.[56]. shRNA sequences and sources are described in Supplementary Table 4.

Lentiviral vectors encoding mitoDsRed (Addgene, 44386), enhanced GFP (eGFP)[57], mito-GFP (Addgene, 44385) and shRNA against *GAP43* (ref. 24) were prepared and titrated according to a protocol reported previously[58]. The mitochondria donor cells were transduced with pLV-mitoDsRed. The acceptor cells were transduced with a lentiviral eGFP vector[57] or, for indicated in vivo experiments, with pLV-mito-GFP.

Human cell co-culture mitochondria transfer assessment by flow cytometry

L1, DI318 and 3832 cells were cultured in tissue culture vessels (adherent) precoated with Geltrex (Thermo Fisher Scientific; 1:250 in serum-free medium overnight) in 90% complete Neurobasal + 10% NSC medium for 4 d, unless otherwise indicated. For *GAP43*-knockdown experiments, co-culture time was reduced to 24 h to reduce the confounding effect of different growth rates in control versus knockdown GBM cells, and comparisons were made between co-cultures with similar astrocyte:tumor cell ratios. Growth factor-reduced Matrigel (Corning) was used as a coating reagent to attach P3, BG5, BG7 and GG16 GBM cells and normal human astrocytes.

The following inhibitors were used: cytochalasin B (Sigma, C6762) and vincristine sulfate (Sigma, V8388). An equivalent amount of vehicle (DMSO) was used as a control. Cell viability was assessed with a LIVE/DEAD Fixable Blue Dead Cell staining kit.

For viability testing of P3 in the presence of inhibitor, GBM cells were seeded at 5,000 cells per Matrigel-coated well of a 96-well plate in 150 µl of complete Neurobasal medium. After incubation with cytochalasin B for 24 h, cell proliferation reagent WST-1 (Roche, CELLPRO-RO) was added, and sample absorbance measurements at 450 nM were determined on a multiscan FC microplate photometer (Thermo Scientific).

For transwell experiments, human-derived GBM cells were plated on Geltrex-coated tissue culture wells. Under 'contact' conditions, human mito-mCherry astrocytes were simultaneously added to the culture well. Under 'transwell' conditions, an equal number of astrocytes was plated in a transwell insert (5-µm pore size, Corning), which was submerged in the culture medium of the underlying culture well.

Co-culture experiments were analyzed on a BD LSR Fortessa or BD FACS Symphony S6 (BD Biosciences) operated by BD FACSDiva software (v8.0 or v9.0). FlowJo software (BD Biosciences, v10.7.2 or 10.8.1) was used to analyze flow cytometry data. The gating strategy is described in Supplementary Fig. 1.

Mouse tumor cell maintenance and transduction

SB28 cells were a gift from H. Okada (University of California, San Francisco). GL261 cells were obtained from the Developmental Therapeutics Program, National Cancer Institute. All cell lines were treated with 1:100 MycoRemoval Agent (MP Biomedicals) after thawing and were routinely tested for *Mycoplasma* spp. (Lonza). Cells were maintained in RPMI 1640 (Media Preparation Core, Cleveland Clinic) supplemented with 10% FBS (Thermo Fisher Scientific) and 1 U ml^{-1} penicillin + 1 µg ml^{-1} streptomycin (Cleveland Clinic Media Preparation Core), that is, non-stem-promoting conditions. For the generation of GFP-expressing GL261 cells, parental GL261 cells were transduced with pReceiver-Lv207 (Genecopoeia) and were selected with 300 µg ml^{-1} hygromycin B (Invitrogen). GFP expression was confirmed by flow cytometry.

Mice

Tg(CAG-mKate2)1Poche/J (mito::mKate2; stock 032188) mice were purchased from The Jackson Laboratory and were housed in the Cleveland Clinic Biological Research Unit. Both sexes of mito::mKate2 mice were

intracranially injected at 4–8 weeks of age with 10,000–20,000 SB28 or 100,000 GL261-GFP cells in 5 µl of RPMI null medium into the left cerebral hemisphere 2 mm caudal to the coronal suture and 3 mm lateral to the sagittal suture at a 90° angle with the skull to a depth of 2.5 mm using a stereotaxis apparatus (Kopf). Male NSG mice were bred in-house by the Cleveland Clinic Biological Resources Unit, and tumors were established orthotopically as described above. Mice were fed standard chow (Teklad Global 18% Protein Rodent Diet, 2913, Envigo) and filtered water ad libitum and were housed in forced/filtered air isolator cages containing up to five mice. Mice were maintained on a 12-h light/12-h dark cycle, with a temperature of 20–26 °C and humidity of 30–70%.

Bone marrow transplantation

Four-week-old male mice were treated with 11 Gy radiation in two fractions 3–4 h apart. Reconstitution was achieved by retro-orbital injection of 2×10^6 bone marrow cells from mito::mKate2 mice. Drinking water was supplemented with Sulfatrim (trimethoprim–sulfamethoxazole; Pharmaceutical Associates) during the first 10 d, and mice were monitored for an additional 6 weeks for weight loss and symptoms of infection before tumor inoculation.

Orthotopic xenograft models in nude rats

Immunodeficient nude-RNU rats of both sexes, bred in-house, were fed a diet containing standard pellets (Sniff, V1536-000), had access to water ad libitum and were housed in filtered air isolator cages (Allentown type IV (Rat 1800), HEPA filter) with a 12-h light/12-h dark cycle at 21 °C and ~45% humidity. Stereotactical implantation of tumor cells into the brain has been described previously[57]. To model mitochondria transfer from normal cells to tumor cells, a high-titer mitoDsRed lentivirus was injected into the brain followed by implantation of GFP$^+$ or mito-GFP$^+$ tumor acceptor cells after 7 d. Animals were euthanized with CO_2 and perfused with 0.9% NaCl.

Immunofluorescence

For immunofluorescence analysis, brains were fixed in 4% paraformaldehyde (PFA), dehydrated in a 30% sucrose solution, embedded in optimal cutting temperature compound and snap frozen. Sectioning (10 µm thick) was performed on a Leica CM3050 S precooled to −20 °C before use. Sections were protected from light and frozen at −80 °C. For staining, tissue sections were incubated overnight at 4 °C with the following primary antibodies: monoclonal anti-GFAP, anti-human nestin, anti-F-actin, anti-GAP43, chicken anti-GFP, rabbit anti-phospho-histone H3 and rabbit anti-cleaved caspase-3. The following secondary antibodies were used: goat anti-mouse 647 at room temperature for 120 min, donkey anti-chicken Alexa Fluor 488 overnight at 4 °C and WGA Alexa Fluor 680 (4 µg ml^{-1} in HBSS-T with magnesium and calcium) for 1 h at room temperature.

Cells on coverslips were fixed in 4% PFA and permeabilized with 0.1% Triton X-100 (Sigma) for 20 min at room temperature. Anti-TOMM20 or anti-nestin was incubated overnight at 4 °C. Goat anti-mouse 488 or goat anti-rabbit 647 were incubated for 60 min at room temperature.

Confocal microscopy and time-lapse imaging

Confocal microscopy of stained mouse tissue sections was performed using a Leica SP8. Still-image processing and *z* reconstructions were completed using LasX software (version 3.3; Leica). Image analysis for estimation of mito::mKate2 transfer to GBM cells in vivo was performed using Velocity software (version 6.3; PerkinElmer). The three-dimensional (3D) segmentation algorithms (Supplementary Note) were set to minimize the (1) detection of mKate2 channel noise (using wild-type tissue sections as a negative control) and (2) identification of GFP$^+$ cells not morphologically compatible with tumor cells, likely the result of GFP phagocytosis in the TME (using a relevant size cutoff).

SB28 cells (40,000) were cocultured with 80,000 mito::mKate2 astrocytes in a glass-bottom 35-mm dish (Mat-tek) overnight. Growth medium was replaced with phenol red-free NSC medium. Multiple full-thickness *z* stacks were obtained every 10 min using a Leica SP8 microscope in a 37 °C chamber supplemented with 5% CO_2 and 95% humidity using a ×20/0.8-NA objective lens. Time-lapse frames were subsequently analyzed by LasX software.

L1 and DI318 cells were stained with CellTrace Green (Thermo Fisher) at 5 µM in serum-free medium at 37 °C for 30 min and washed with complete Neurobasal medium before plating with human mito-mCherry astrocytes in ibidiTread 35-mm microscopy dishes (Ibidi) that had been coated with Geltrex (Gibco). After 48 h, cells were washed gently with PBS, fixed with 4% PFA for 15 min at 4 °C and imaged by confocal microscopy.

For TOMM20 colocalization experiments, cells were plated as described above and cocultured for 72 h. Cells were then stained with primary antibody (anti-TOMM20; clone D8T4N) for 1 h at room temperature and with secondary anti-rabbit DyLight405 alpaca for 1 h at room temperature. Colocalization analysis (line profile quantification) was performed using Image-Pro Plus 10 (Media Cybernetics).

Confocal imaging for P3, BG5, BG7 and GG16 co-culture experiments was performed using a Leica TCS SP8 STED 3X (Leica Microsystems) run by LasX software (version 3.3, Leica, version LAS4.13). Image analyses were performed with ImageJ (v2.3.0/1.53f) and Imaris (v9.6).

Measurement of mitochondrial trafficking in vivo by flow cytometry

Resected tumors or the contralateral hemisphere were digested with 1 mg ml^{-1} collagenase IV (StemCell Technologies) and 1 mg ml^{-1} DNase I (Roche) for 15 min at 37 °C. Samples were strained through a 100-µm strainer (Fisherbrand) and washed with PBS. Cells were stained with a LIVE/DEAD Fixable Blue Dead Cell Stain kit (Thermo Fisher Scientific) for 10 min on ice, treated with FcR blocking reagent (Miltenyi Biotec) diluted 1:50 for 15 min on ice and stained with 1:100 APC-conjugated anti-CD11b (BioLegend, clone M1/70) for 20 min to exclude phagocytic cells. Samples were fixed overnight with a eBioscience FoxP3 transcription factor fixation kit (Thermo Fisher Scientific) and analyzed with a BD LSRII Fortessa (BD Biosciences) in PBS.

Generation of mouse astrocytes and microglia and in vitro mouse mitochondria transfer assay

Brain-resident glial cell cultures were obtained, as previously described[59], by resecting the subventricular zone of brains from postnatal day 0–3 mice and culturing in NSC medium. Microglia were generated by culturing confluent monolayers of early passage (passage 2 or 3) glial cell cultures with microglia polarization medium (DMEM-F12, 1 U ml^{-1} penicillin + 1 µg ml^{-1} streptomycin, 10% FBS and 20 ng ml^{-1} granulocyte–macrophage colony-stimulated factor (BioLegend)). After 5 d, microglia (loosely adherent) were obtained by agitation of the culture flask on an orbital shaker for 45 min.

A total of 20,000–40,000 astrocytes and microglia were separately cultured in a 96-well flat-bottom plate in NSC medium or microglia polarization medium, respectively. Forty-eight hours later, supernatants were collected and centrifuged at 400*g* for 5 min to remove residual cells; these supernatants consisted of the conditioned, cell-free culture medium. Tumor cells were added at a recipient: donor ratio of 2:1 to the adherent donor cell cultures to assess total mitochondria transfer (contact dependent and independent); separately, tumor cells alone were cultured with conditioned, cell-free medium described above to assess contact-independent (secreted) mitochondria transfer. Samples were incubated for 2 h and treated with Accutase to generate single-cell suspensions. Cells were transferred to 96-well U-bottom plates to stain with LIVE/DEAD dye. Exogenous mitochondria uptake by GFP$^+$ tumor cells was assessed with a BD LSRII Fortessa.

Generation of mouse macrophages and in vitro mitochondria uptake assay

Bone marrow from the femurs and tibiae of 4- to 8-week-old male and female mito::mKate2 mice was flushed with PBS using a 27-gauge needle. Eighty thousand cells were cultured in 24-well plates and treated with 50 ng ml^{-1} recombinant mouse macrophage colony-stimulating factor (BioLegend) in IMDM (Media Preparation Core) supplemented with 1 U ml^{-1} penicillin + 1 µg ml^{-1} streptomycin and 20% FBS for 6 d. Interferon-γ or interleukin-4 (50 ng ml^{-1}; BioLegend) was added for 48 h to further induce polarization of macrophages to M1- or M2-like macrophages, respectively. Supernatants were collected and centrifuged at 400*g* for 5 min to remove residual cells and to generate conditioned, cell-free culture medium. Tumor cells were added at twofold abundance in technical duplicates for a 2-h incubation, as described above, to test contact-dependent versus contact-independent mitochondria transfer. Samples were incubated with Accutase for 5 min and transferred into 96-well U-bottom plates for staining with the viability dye and anti-CD11b as described above. Exogenous mitochondria uptake was analyzed in GFP$^+$ tumor cells using a BD LSRII Fortessa.

Western blotting

Cells were washed twice with PBS and dissolved in lysis buffer (10 mM Tris-HCl (pH 7.4), 150 mM NaCl, 0.5% NP-40, 1% Triton X-100 and 1 mM EDTA) supplemented with protease and phosphatase inhibitor cocktails (Roche). Protein concentration was quantified by Bradford assay (Euromedex). Cell lysates were resuspended in Laemmli buffer (62.5 mM Tris (pH 6.8), 10% glycerol, 2.5% SDS and 2.5% β-mercaptoethanol). The primary antibody was anti-GAP43, the housekeeping protein vinculin was used as the loading control and the secondary antibody was goat anti-rabbit horseradish peroxidase (HRP; Invitrogen, 31462). Membranes were developed on a LAS 3000 (version 2.2; Fujifilm).

For GAP43 blots (Extended Data Fig. 6i,j) and stem cell transcription factors (Extended Data Fig. 10b), cells were lysed with ice-cold RIPA buffer. The following primary antibodies were used: anti-GAP43, anti-actin, anti-SOX2 and anti-OCT4. Secondary antibodies were goat anti-rabbit HRP or goat anti-mouse HRP.

Sorting of tumor cells from co-cultures

For mouse GBM models, astrocytes were collected from flasks by Accutase treatment and stained with a 1:1,000 dilution of CellTrace Violet cell proliferation dye in PBS at 37 °C for 20 min. Tumor cells and astrocytes were then cocultured at a 1:1 ratio for 48 h in NSC medium. Samples were sorted into RPMI with 20% FBS and cultured overnight in complete RPMI for subsequent functional assays.

For collection of double-positive or single-positive cells in co-cultures of P3, BG5 and GG16 GBM cells with immortalized mitoDsRed normal human astrocytes by cell sorting, 2×10^6 cells of each cell line were seeded in Neurobasal medium on Matrigel (T75 flasks). For analyzing mitochondria transfer by flow cytometry, 1.5×10^5 cells from each cell line were seeded in Neurobasal medium on Matrigel (T25 flasks). L1 and DI318 cells were sorted after 4 d of co-culture with immortalized mito-mCherry human astrocytes from Geltrex-coated flasks (seeded at 1:1 and 1:1.5 donor:recipient ratio, respectively, to adjust for differences in cell growth rate).

In vitro limiting dilution assay

Sorted tumor cells were cultured at decreasing cell densities over 12 technical replicates in complete Neurobasal medium, and the number of wells containing spheres was counted after 11–14 d. For the mouse cell line SB28, 400 to 25 cells per well of a 96-well plate were seeded; for human lines, this ranged from 100 to 1.25 cells per well. The online ELDA tool (http://bioinf.wehi.edu.au/software/elda/, 24 October 2014 version) was used to calculate stem cell frequency[60].

In vivo limiting dilution/tumor initiation assays

Sorted mouse/human GBM cells with and without the acquisition of astrocyte mitochondria in vitro were counted with trypan blue using a TC-20 cell counter (Bio-Rad) and were volume adjusted to achieve decreasing cell concentrations (18,000–1,000, as indicated) for intracranial implantation. Subsequently, C57BL/6 mice (mouse GBM models) or NSG mice (human GBM models) were intracranially implanted with equal numbers of tumor cells, as described above. The identity of the implanted cells was then blinded to investigators. Mice were euthanized at humane endpoints (neurological symptoms, weight loss, poor grooming or any other sign of distress).

Seahorse assay

For sorted P3 GFP mitoDsRed$^+$ and mitoDsRed$^-$ cells, mitochondrial respiration assays were performed using 3.0 mM oligomycin, 1.5 mM carbonyl cyanide m-chlorophenyl hydrazone (CCCP), 1.0 mM rotenone and 1.0 mM antimycin A in assay medium consisting of unbuffered, phenol red-free DMEM with 10 mM glucose, 2 mM sodium pyruvate and 4 mM L-glutamine with a pH of 7.4. Cells were incubated for 60 min in a Prep Station (Agilent) under non-CO_2 conditions at 37 °C and were subsequently placed in the Seahorse Xfe96 analyzer. The chemical compounds were serially injected to manipulate the cells and create metabolic flux reports. Data were analyzed using Agilent Seahorse Wave Controler v2.6.3, IDEAS software (version 6.2; EMD Millipore).

ATP quantification

CellTiter-Glo reagent (100 µl; Promega) was added to cells and incubated on an orbital shaker at room temperature for 20–30 min. ATP levels were quantified indirectly by relative luminescence intensity measured on a Victor 3 plate reader (PerkinElmer).

Metabolic protein flow cytometry analysis

For mouse cells, the metabolic protein flow cytometry panel was adapted from Ahl et al.[40]. CellTrace Violet-stained astrocytes were cocultured with tumor cells overnight at a 1:1 ratio. Samples were fixed in eBioscience FoxP3 transcription factor fixation buffer for 30 min on ice and stained with the following antibodies in 1× permeabilization buffer for 30 min at room temperature: anti-argininosuccinate synthetase 1 (ASS1), anti-ATP synthase F1 subunit α (ATP5A), anti-glucose transporter 1 (GLUT1), anti-isocitrate dehydrogenase 2 (IDH2), anti-glucose 6 phosphate dehydrogenase (G6PD), anti-acetyl-CoA carboxylase (ACC1), anti-peroxiredoxin 2 (PRDX2), anti-hexokinase 1 (HK1), anti-carnitine palmitoyltransferase I (CPT1A), anti-SLC20A1, anti-mouse IgG1 (κ monoclonal), anti-mouse IgG2b (κ monoclonal) and rabbit IgG (monoclonal). Samples were washed and resuspended in 1× permeabilization buffer containing goat anti-mouse IgG H&L (Alexa Fluor 647) or donkey anti-rabbit IgG H&L (Alexa Fluor 647). After 30 min of incubation at room temperature, cells were washed with permeabilization buffer and resuspended in PBS for analysis with a BD LSRII Fortessa. Geometric mean fluorescence intensity was used to calculate expression levels after subtraction of the background levels from isotype control staining.

The same procedure was used for human cell metabolic flow, with minor modifications. Seven different human-derived cell lines were cocultured with human mito-mCherry astrocytes for 4 d. Most antibodies listed above cross-reacted with human antigens and were thus also used in these experiments, with the exception of using directly conjugated Alexa Fluor 647 antibodies for ATP5A and GLUT1.

Metabolomics analysis

Sorted mouse GBM cell pellets were resuspended in 80% ice-cold methanol for metabolite extraction and sent to an academic core facility for targeted metabolomics (Beth Israel Deaconess Mass Spectrometry Core Facility, Harvard Medical School). Data were normalized by peak count. Values of zero (below the limit of quantitation) were

substituted with the approximate limit of quantitation (2,000 peak count) to facilitate fold change analysis. Metabolites enriched by >20% in mKate2$^+$ GBM cells were put into the metabolic pathway enrichment analysis algorithm MetaboAnalyst 5.0 web tool (www.metaboanalyst.ca)[61]. The following analysis settings were used: HMDB and KEGG compound names; feature type = metabolites; KEGG analysis.

For human GSCs, triplicate cell pellet samples were lysed in 80:20 methanol:water at dry ice temperature. The quantity of the metabolite fraction analyzed was adjusted to the cell count. Extracts were clarified by centrifugation, dried by nitrogen blower and reconstituted in equal volumes 50:50 methanol:water. Metabolite fractions were analyzed by targeted liquid chromatography–tandem mass spectrometry via dynamic multiple reaction monitoring. An Agilent Technologies Triple Quad 6470 liquid chromatography–tandem mass spectrometry system, consisting of the 1290 Infinity II LC flexible pump (Quaternary Pump), the 1290 Infinity II multisampler, the 1290 Infinity II multicolumn thermostat with six-port valve and the 6470 triple quad mass spectrometer, was used for analysis. Agilent MassHunter Workstation software LC/MS data acquisition for 6400 Series Triple Quadrupole MS with version B.08.02 was used for compound optimization and sample data acquisition. Studies were performed in negative ion acquisition mode with ion-pairing chromatography using an Agilent ZORBAX RRHD Extend-C18, 2.1 × 150 mm, 1.8 µm and ZORBAX Extend Fast Guards for UHPLC separation. Agilent MassHunter Workstation quantitative analysis for QQQ version 10.1, build 10.1.733.0, was used to integrate and quantitate metabolite peak areas. Liquid chromatography–mass spectrometry peaks corresponding to metabolites with coefficients of variation greater than 0.5 underwent manual inspection and integration. The data were normalized to the average sum of metabolites from all the samples and were analyzed using Morpheus to generate the heat map. Metaboanalyst was used to compare metabolites and metabolic pathways enriched in mito-mCherry$^+$ L1 cells and mito-mCherry$^-$ L1 cells.

Phosphoprotein array

Human-derived GBM cells (L1) were cocultured with human mito-mCherry astrocytes for 4 d and flow sorted to obtain mCherry$^+$ and mCherry$^-$ GBM cells. Sorted cell pellets were flash-frozen in liquid nitrogen and sent for a commercial microarray platform, antibody-based phosphoprotein array (Phospho Explorer array, FullMoon BioSystems). The complete antibody list can be found in Supplementary Table 3. Analysis was conducted using the phosphorylation ratio of each protein for samples tested (phosphorylated protein signal divided by corresponding total protein signal). We analyzed the functional enrichment of the upregulated phosphoproteins using Enrichr[62] against the Gene Ontology (GO) biological process term data set. GO terms with FDR values of <0.05 were considered significantly enriched. We summarized the enriched terms using Revigo[63] to generate a graph-based view of the subdivisions of the terms.

ImageStream

A clone of HEK293T cells able to grow in serum-free medium (CSC293T) was generated and cultured as previously described[64]. CSC293T cells were transfected with psPAX2, pCMV-VSVG and pLYS1-Mito-GFP or pCMV-RFP using FuGENE HD transfection reagent (Promega). Viral concentration was determined using the Lenti-X qRT–PCR titration kit (Takara Bio). Immortalized normal human astrocytes were transduced with mito-GFP lentivirus and selected for cells stably expressing mito-GFP using puromycin. D456 and JX22 cells were transduced with RFP lentivirus and selected using blasticidin S (Gibco) to select for stable RFP-expressing cells. Where indicated, cells were sorted for mito-GFP positivity or RFP positivity with assistance from the Flow Cytometry Core at the University of Alabama at Birmingham.

RFP-expressing D456 or JX22 cells were cocultured at a 1:1 ratio in the presence of mito-GFP$^+$ astrocytes for 24 h. Samples were imaged at ×40 magnification with extended depth of field. Mito-GFP was acquired on ch02, and RFP was acquired on ch04. Ch01 and ch09 were used for brightfield imaging, and ch12 was used for side scatter. Five thousand events were recorded, and relevant single-color and unstained controls were used. Data were analyzed using IDEAS software (version 6.2; EMD Millipore).

RNA-seq

mKate$^+$ and mKate$^-$ SB28 cells and astrocytes from three distinct co-cultures (biological replicates) were sorted into multiple 1.5-ml DNA LoBind microtubes (Eppendorf), each containing 700 µl of RLT Plus lysis buffer (Qiagen) supplemented with 1% β-mercaptoethanol. RNA isolation was performed using the RNEasy Plus Micro kit (Qiagen).

RNA-seq and analysis were performed by GENEWIZ. Briefly, samples were sequenced using an Illumina HiSeq, with a 2 × 150 base pair configuration and ≥350 million raw paired-end reads. An average of 41.6 million paired-end reads was sequenced across nine samples. After Illumina universal adapters were trimmed, the reads were mapped to the *Mus musculus* GRCm38 reference genome using the STAR aligner v.2.5.2b. Unique gene hit counts were calculated by using featureCounts from the Subread package v.1.5.2.

For comparison of tumor cells with astrocytes, genes with an adjusted P value of <0.05 and absolute $\log_2$ (fold change) of >1 were called as differentially expressed genes (DEGs) using DESeq2. For assessment of differentially upregulated pathways in mKate$^+$ versus mKate$^-$ SB28 cells, genes that were upregulated >1.5-fold with a count number >50 and an unadjusted P value of <0.05 (Supplementary Table 1) were plugged into https://maayanlab.cloud/Enrichr/.

Protein–protein interactions and network visualization

Differential expression analysis was performed using edgeR 3.34 (ref. 65). Genes with a count per million greater than 1 in at least two samples were used for the analysis. P values of <0.05 were considered significant. The mouse DEGs were mapped to the human homologs using the NCBI HomoloGene database (https://www.ncbi.nlm.nih.gov/homologene). We then performed the enrichment analysis using Enrichr[62] for the entire set of DEGs and for the up- and downregulated genes separately.

The protein–protein interactions among the DEGs were extracted using a human protein interactome we built previously[66] that contains 17,706 protein nodes and 351,444 protein–protein interaction edges. We then visualized this protein–protein interaction network using Cytoscape 3.8 (ref. 67). Genes that localize to mitochondria are indicated by a diamond node shape based on the Human MitoCarta2.0 database[68].

Cell cycle analysis

Single-cell suspensions (from mouse tumors or cultured cells) were fixed in PBS with 4% PFA for 1 h on ice and washed with permeabilization buffer (Foxp3/transcription factor staining buffer set; Ebioscience). Subsequently, cells were stained with Hoechst 33342 (Thermo Fisher) at 3.33 µg ml^{-1} in PBS for 1 h at room temperature, washed with PBS supplemented with 2% bovine serum albumin and assayed by flow cytometry.

Mitochondria isolation

Mitochondria were isolated from confluent immortalized human astrocyte cultures expressing mCherry by using the mitochondria isolation kit for cultured cells (Thermo Fisher Scientific), as per the manufacturer's instructions. Mitochondria were quantified by total protein using the Qubit protein assay kit (Thermo Fisher), according to the manufacturer's protocol.

Quantification of phospho-histone H3 and cleaved caspase-3 immunofluorescence

To quantify elements within the TME, tissue was examined from three animals per biological sex per mitochondrial transfer status. For a

given animal, 15 representative images were captured (5 images × 3 tumor-bearing sections). Cellular proliferation was quantified by counting each phosphorylated histone $H3^+$ nucleus in each visual field. This count was divided by the fluorescence intensity of the GFP signal of the same field to account for variation in tumor size and cellular density to yield a mitotic index. The apoptotic cell death index was quantified by dividing the fluorescence intensity of the cleaved caspase-3 signal by the fluorescence intensity of the GFP signal in the same visual field.

MT quantifications

MT number was quantified manually using the NIH ImageJ software. DAPI and nestin-immunostained confocal images magnified ×200 were used. For each experimental condition, a minimum of 80–120 MTs showing a direct connection between two tumor cells was included for measurement. All measured data were exported into Microsoft Excel and GraphPad Prism 8.1.2 for further calculation of statistical significance.

Statistics and reproducibility

For most in vitro experiments, a minimum of three biologically independent samples was used per experimental group; power was not calculated. For in vivo experiments not involving tumor initiation capacity, sample size was determined based on minimum utilization of vertebrate animals and high expected magnitude of effect without formal power evaluation. For in vivo experiments involving tumor initiation analysis, sample size was determined by prior experience and application of this assay in stem cell biology studies, for example, in Karunanithi et al.[69]. No data were excluded from analyses. Key findings were replicated across time, by different institutions, using diverse models. For survival/tumor initiation studies, mice were randomized before tumor implantation, and investigators were blinded to the grouping. Data distribution was assumed to be normal, but this was not formally tested.

Data representation and analysis

Flow cytometry data were analyzed and generated using FlowJo software (BD Biosciences, v10.7.2). Graphs were generated and statistical analyses were performed using Excel (Microsoft Office, v16.52) or Prism (GraphPad, v9.2.0) software. All measurements shown represent distinct samples, unless otherwise indicated. All statistical tests are two tailed and corrected for multiple comparisons, unless otherwise indicated.

Reporting summary

Further information on research design is available in the Nature Portfolio Reporting Summary linked to this article.

Data availability

Sequencing files have been deposited to Gene Expression Omnibus under accession number GSE183004. Metabolic pathway analysis was based on the KEGG human metabolic pathways database (October 2019; https://www.genome.jp/kegg/pathway.html#metabolism). Protein phosphorylation array data were mapped to pathways based on the GO biological process term data set (http://geneontology.org/). RNA-seq reads of mouse cells were mapped to the *M. musculus* GRCm38 reference genome (https://www.ncbi.nlm.nih.gov/assembly/GCF_000001635.20/). The RNA-seq inferred protein–protein interaction network was constructed by mapping to human homologs using the NCBI HomoloGene database (https://www.ncbi.nlm.nih.gov/homologene). Genes encoding mitochondria-localizing proteins were identified with MitoCarta2.0 (https://www.broadinstitute.org/files/shared/metabolism/mitocarta/human.mitocarta2.0.html). All other data are available in the main text or the Supplementary Information. Source data are provided with this paper.

References

1. Bock, F. J. & Tait, S. W. G. Mitochondria as multifaceted regulators of cell death. *Nat. Rev. Mol. Cell Biol.* **21**, 85–100 (2020).
2. Giacomello, M., Pyakurel, A., Glytsou, C. & Scorrano, L. The cell biology of mitochondrial membrane dynamics. *Nat. Rev. Mol. Cell Biol.* **21**, 204–224 (2020).
3. Jones, W. & Bianchi, K. Aerobic glycolysis: beyond proliferation. *Front. Immunol.* **6**, 227 (2015).
4. Hay, N. Reprogramming glucose metabolism in cancer: can it be exploited for cancer therapy? *Nat. Rev. Cancer* **16**, 635–649 (2016).
5. Poteet, E. et al. Reversing the Warburg effect as a treatment for glioblastoma. *J. Biol. Chem.* **288**, 9153–9164 (2013).
6. Hoang-Minh, L. B. et al. Infiltrative and drug-resistant slow-cycling cells support metabolic heterogeneity in glioblastoma. *EMBO J.* **37**, e98772 (2018).
7. Talasila, K. M. et al. The angiogenic switch leads to a metabolic shift in human glioblastoma. *Neuro Oncol.* **19**, 383–393 (2017).
8. Friedmann-Morvinski, D. Glioblastoma heterogeneity and cancer cell plasticity. *Crit. Rev. Oncog.* **19**, 327–336 (2014).
9. Lauko, A., Lo, A., Ahluwalia, M. S. & Lathia, J. D. Cancer cell heterogeneity & plasticity in glioblastoma and brain tumors. *Semin. Cancer Biol.* **82**, 162–175 (2021).
10. Perrin, S. L. et al. Glioblastoma heterogeneity and the tumour microenvironment: implications for preclinical research and development of new treatments. *Biochem. Soc. Trans.* **47**, 625–638 (2019).
11. Yin, J. et al. Exosomal transfer of miR-1238 contributes to temozolomide-resistance in glioblastoma. *eBioMedicine* **42**, 238–251 (2019).
12. Knudsen, A. M., Rudkjobing, S. J., Sorensen, M. D., Dahlrot, R. H. & Kristensen, B. W. Expression and prognostic value of the immune checkpoints galectin-9 and PD-L1 in glioblastomas. *J. Neuropathol. Exp. Neurol.* **80**, 541–551 (2021).
13. Broekman, M. L. et al. Multidimensional communication in the microenvirons of glioblastoma. *Nat. Rev. Neurol.* **14**, 482–495 (2018).
14. Hayakawa, K. et al. Transfer of mitochondria from astrocytes to neurons after stroke. *Nature* **535**, 551–555 (2016).
15. Phinney, D. G. et al. Mesenchymal stem cells use extracellular vesicles to outsource mitophagy and shuttle microRNAs. *Nat. Commun.* **6**, 8472 (2015).
16. Wang, X. & Gerdes, H. H. Transfer of mitochondria via tunneling nanotubes rescues apoptotic PC12 cells. *Cell Death Differ.* **22**, 1181–1191 (2015).
17. Torralba, D., Baixauli, F. & Sanchez-Madrid, F. Mitochondria know no boundaries: mechanisms and functions of intercellular mitochondrial transfer. *Front. Cell Dev. Biol.* **4**, 107 (2016).
18. Zou, X. et al. Mitochondria transfer via tunneling nanotubes is an important mechanism by which $CD133^+$ scattered tubular cells eliminate hypoxic tubular cell injury. *Biochem. Biophys. Res. Commun.* **522**, 205–212 (2020).
19. Rustom, A., Saffrich, R., Markovic, I., Walther, P. & Gerdes, H. H. Nanotubular highways for intercellular organelle transport. *Science* **303**, 1007–1010 (2004).
20. Ranzinger, J. et al. Nanotube action between human mesothelial cells reveals novel aspects of inflammatory responses. *PLoS ONE* **6**, e29537 (2011).
21. Abounit, S. & Zurzolo, C. Wiring through tunneling nanotubes—from electrical signals to organelle transfer. *J. Cell Sci.* **125**, 1089–1098 (2012).
22. Roehlecke, C. & Schmidt, M. H. H. Tunneling nanotubes and tumor microtubes in cancer. *Cancers* **12**, 857 (2020).
23. Osswald, M., Solecki, G., Wick, W. & Winkler, F. A malignant cellular network in gliomas: potential clinical implications. *Neuro Oncol.* **18**, 479–485 (2016).
24. Osswald, M. et al. Brain tumour cells interconnect to a functional and resistant network. *Nature* **528**, 93–98 (2015).

25. Weil, S. et al. Tumor microtubes convey resistance to surgical lesions and chemotherapy in gliomas. *Neuro Oncol.* **19**, 1316–1326 (2017).
26. Jung, E. et al. Tweety-homolog 1 drives brain colonization of gliomas. *J. Neurosci.* **37**, 6837–6850 (2017).
27. Joseph, J. V. et al. TGF-β promotes microtube formation in glioblastoma through thrombospondin 1. *Neuro Oncol.* **24**, 541–553 (2021).
28. Shen, Y., Mani, S., Donovan, S. L., Schwob, J. E. & Meiri, K. F. Growth-associated protein-43 is required for commissural axon guidance in the developing vertebrate nervous system. *J. Neurosci.* **22**, 239–247 (2002).
29. da Silva, B. et al. Chemically induced neurite-like outgrowth reveals a multicellular network function in patient-derived glioblastoma cells. *J. Cell Sci.* **132**, jcs228452 (2019).
30. Barrasso, A. P., Tong, X. & Poche, R. A. The mito::mKate2 mouse: a far-red fluorescent reporter mouse line for tracking mitochondrial dynamics in vivo. *Genesis* **56**, e23087 (2018).
31. Tsai, I. J., Su, E. C., Tsai, I. L. & Lin, C. Y. Clinical assay for the early detection of colorectal cancer using mass spectrometric wheat germ agglutinin multiple reaction monitoring. *Cancers* **13**, 2190 (2021).
32. Venkataramani, V. et al. Glioblastoma hijacks neuronal mechanisms for brain invasion. *Cell* **185**, 2899–2917 (2022).
33. Salaud, C. et al. Mitochondria transfer from tumor-activated stromal cells (TASC) to primary glioblastoma cells. *Biochem. Biophys. Res. Commun.* **533**, 139–147 (2020).
34. Joseph, J. V. et al. TGF-β promotes microtube formation in glioblastoma through thrombospondin 1. *Neuro Oncol.* **24**, 541–553 (2022).
35. Valdebenito, S. et al. Tunneling nanotubes, TNT, communicate glioblastoma with surrounding non-tumor astrocytes to adapt them to hypoxic and metabolic tumor conditions. *Sci Rep.* **11**, 14556 (2021).
36. Pinto, G. et al. Patient-derived glioblastoma stem cells transfer mitochondria through tunneling nanotubes in tumor organoids. *Biochem. J.* **478**, 21–39 (2021).
37. Civita, P., Leite, D. M. & Pilkington, G. J. Pre-clinical drug testing in 2D and 3D human in vitro models of glioblastoma incorporating non-neoplastic astrocytes: tunneling nano tubules and mitochondrial transfer modulates cell behavior and therapeutic response. *Int. J. Mol. Sci.* **20**, 6017 (2019).
38. He, Q., Dent, E. W. & Meiri, K. F. Modulation of actin filament behavior by GAP-43 (neuromodulin) is dependent on the phosphorylation status of serine 41, the protein kinase C site. *J. Neurosci.* **17**, 3515–3524 (1997).
39. Nguyen, L., He, Q. & Meiri, K. F. Regulation of GAP-43 at serine 41 acts as a switch to modulate both intrinsic and extrinsic behaviors of growing neurons, via altered membrane distribution. *Mol. Cell. Neurosci.* **41**, 62–73 (2009).
40. Ahl, P. J. et al. Met-Flow, a strategy for single-cell metabolic analysis highlights dynamic changes in immune subpopulations. *Commun. Biol.* **3**, 305 (2020).
41. Spinelli, J. B. & Haigis, M. C. The multifaceted contributions of mitochondria to cellular metabolism. *Nat. Cell Biol.* **20**, 745–754 (2018).
42. Baines, C. P. et al. Mitochondrial PKCε and MAPK form signaling modules in the murine heart: enhanced mitochondrial PKCε–MAPK interactions and differential MAPK activation in PKCε-induced cardioprotection. *Circ. Res.* **90**, 390–397 (2002).
43. Bohovych, I. & Khalimonchuk, O. Sending out an SOS: mitochondria as a signaling hub. *Front. Cell Dev. Biol.* **4**, 109 (2016).
44. Wang, X. et al. Targeting pyrimidine synthesis accentuates molecular therapy response in glioblastoma stem cells. *Sci. Transl. Med.* **11**, eaau4972 (2019).
45. Wang, X. et al. Purine synthesis promotes maintenance of brain tumor initiating cells in glioma. *Nat. Neurosci.* **20**, 661–673 (2017).
46. Chisari, A. et al. Glucose and amino acid metabolic dependencies linked to stemness and metastasis in different aggressive cancer types. *Front. Pharmacol.* **12**, 723798 (2021).
47. McBrayer, S. K. et al. Transaminase inhibition by 2-hydroxyglutarate impairs glutamate biosynthesis and redox homeostasis in glioma. *Cell* **175**, 101–116 (2018).
48. Zhou, W. et al. Purine metabolism regulates DNA repair and therapy resistance in glioblastoma. *Nat. Commun.* **11**, 3811 (2020).
49. Caicedo, A. et al. MitoCeption as a new tool to assess the effects of mesenchymal stem/stromal cell mitochondria on cancer cell metabolism and function. *Sci. Rep.* **5**, 9073 (2015).
50. Dong, L. F. et al. Horizontal transfer of whole mitochondria restores tumorigenic potential in mitochondrial DNA-deficient cancer cells. *eLife* **6**, e22187 (2017).
51. Pasquier, J. et al. Preferential transfer of mitochondria from endothelial to cancer cells through tunneling nanotubes modulates chemoresistance. *J. Transl. Med.* **11**, 94 (2013).
52. Marlein, C. R. et al. CD38-driven mitochondrial trafficking promotes bioenergetic plasticity in multiple myeloma. *Cancer Res.* **79**, 2285–2297 (2019).
53. Guryanova, O. A. et al. Nonreceptor tyrosine kinase BMX maintains self-renewal and tumorigenic potential of glioblastoma stem cells by activating STAT3. *Cancer Cell* **19**, 498–511 (2011).
54. Deleyrolle, L. P. et al. Evidence for label-retaining tumour-initiating cells in human glioblastoma. *Brain* **134**, 1331–1343 (2011).
55. Sundar, S. J. et al. Three-dimensional organoid culture unveils resistance to clinical therapies in adult and pediatric glioblastoma. *Transl. Oncol.* **15**, 101251 (2022).
56. Tiscornia, G., Singer, O. & Verma, I. M. Production and purification of lentiviral vectors. *Nat. Protoc.* **1**, 241–245 (2006).
57. Huszthy, P. C. et al. Remission of invasive, cancer stem-like glioblastoma xenografts using lentiviral vector-mediated suicide gene therapy. *PLoS ONE* **4**, e6314 (2009).
58. Hossain, J. A., Riecken, K., Miletic, H. & Fehse, B. Cancer suicide gene therapy with TK.007. *Methods Mol. Biol.* **1895**, 11–26 (2019).
59. Marshall, G. P. II, Demir, M., Steindler, D. A. & Laywell, E. D. Subventricular zone microglia possess a unique capacity for massive in vitro expansion. *Glia* **56**, 1799–1808 (2008).
60. Hu, Y. & Smyth, G. K. ELDA: extreme limiting dilution analysis for comparing depleted and enriched populations in stem cell and other assays. *J. Immunol. Methods* **347**, 70–78 (2009).
61. Pang, Z. et al. MetaboAnalyst 5.0: narrowing the gap between raw spectra and functional insights. *Nucleic Acids Res.* **49**, W388–W396 (2021).
62. Kuleshov, M. V. et al. Enrichr: a comprehensive gene set enrichment analysis web server 2016 update. *Nucleic Acids Res.* **44**, W90–W97 (2016).
63. Supek, F., Bosnjak, M., Skunca, N. & Smuc, T. REVIGO summarizes and visualizes long lists of gene ontology terms. *PLoS ONE* **6**, e21800 (2011).
64. Walker, K. & Hjelmeland, A. Method for efficient transduction of cancer stem cells. *J. Cancer Stem Cell Res.* **2**, e1008 (2014).
65. Robinson, M. D., McCarthy, D. J. & Smyth, G. K. edgeR: a Bioconductor package for differential expression analysis of digital gene expression data. *Bioinformatics* **26**, 139–140 (2010).
66. Cheng, F. et al. Network-based approach to prediction and population-based validation of in silico drug repurposing. *Nat. Commun.* **9**, 2691 (2018).
67. Shannon, P. et al. Cytoscape: a software environment for integrated models of biomolecular interaction networks. *Genome Res.* **13**, 2498–2504 (2003).

68. Calvo, S. E., Clauser, K. R. & Mootha, V. K. MitoCarta2.0: an updated inventory of mammalian mitochondrial proteins. *Nucleic Acids Res.* **44**, D1251–D1257 (2016).
69. Karunanithi, S. et al. RBP4–STRA6 pathway drives cancer stem cell maintenance and mediates high-fat diet-induced colon carcinogenesis. *Stem Cell Rep.* **9**, 438–450 (2017).

Acknowledgements

We thank A. Mendelsohn for illustrations; the LRI Flow Cytometry Core (an ISAC-recognized Shared Resource Laboratory), the LRI Imaging Core, J. Peterson, A. Mulya, S. Prasad, B. Nordanger and H. S. Saed for their technical assistance and discussions; the Molecular Imaging Center and the Flow Cytometry Core Facility in Bergen, Norway, for technical support; F. Kruyt for the GG16 cell line (University of Groningen, Netherlands) and A. Andren and L. Zhang for technical support with metabolomics analysis. This work used flow cytometry and sorting equipment supported with funds from the Clinical and Translational Science Collaborative of Cleveland, UL1TR002548, from the National Center for Advancing Translational Sciences. This work used the Leica SP8 confocal microscope that was purchased with funding from National Institutes of Health SIG grant 1S10OD019972-01. Funding for this study was provided by Lerner Research Institute, Cleveland Clinic (J.D.L.), Case Comprehensive Cancer Center (J.D.L.), National Institutes of Health grant R35 NS127083 (J.D.L.), VeloSano Cancer Research Pilot Award (D.C.W., D.B. and J.D.L.), 2020 VeloSano Trainee Dream Experiment (D.C.W.), National Institutes of Health grants 5T32AI007024 and 5TL1TR002549 (D.C.W.), National Institutes of Health grant K99CA248611 (D.B.), Helse Vest fellowship grant (S.S.), University of Bergen fellowship grant (S.S.M.), The Research Council of Norway grant 325883 (S.S.M. and H.M.), Norwegian Cancer Society grant 197933 (J.H. and H.M.), National Institutes of Health grant K00CA253768 (S.A.S.), National Institutes of Health grant F30CA250254 (A.L.), National Institutes of Health grant F31CA264849 (K.K.) and National Institutes of Health grant F32CA260735 (A.J.S.).

Author contributions

Conceptualization: D.C.W., D.B., J.D.L. and H.M. Methodology: D.C.W., D.B., S.S., S.S.M., S.A.S., J.H., M.T.A., S.E.W., A.L., P. Sravya, Y.Z., S.A.S., K.T., S.W., K.K., D.J.S., E.M.-H., G.D., A.C., G.V.R., K.J.T., K.S., T.R.L., J.V.J., L.A.R.Y., J.G., C.R.M., L.N., J.M., T.D., J.A.H., A.J.S. and P. Sajjakulnukit. Investigation: D.C.W., D.B., S.S., S.S.M., J.H., M.T.A., S.E.W., A.L., P. Sravya, Y.Z., G.D., J.S., S.A.S., K.T., S.W., K.K., D.J.S., S.D., A.C., G.V.R., L.A.R.Y., J.A.H., A.J.S., P. Sajjakulnukit, C.A.L. and D.R.W. Visualization: D.C.W., D.B., S.A.S., S.S.M., J.H., S.E.W., Y.Z., G.D., K.K., D.J.S., S.S. and P. Sravya. Funding acquisition: D.C.W., D.B., J.D.L. and H.M. Project administration: J.D.L. and H.M. Supervision: J.A.M., F.C., A.B.H., J.D.L., H.M., R.B., C.A.L. and D.R.W. Writing, original draft: D.C.W., D.B., J.D.L., S.S., S.S.M. and H.M. Writing, review and editing: D.C.W., D.B., S.S., S.S.M., J.H., S.E.W., A.L., G.D., J.S., J.A.M., Y.Z., F.C., A.B.H., J.D.L., R.B., T.D., P. Sravya, D.R.W., J.A.H. and H.M.

Competing interests

The authors declare no competing interests.

Additional information

Extended data is available for this paper at https://doi.org/10.1038/s43018-023-00556-5.

Supplementary information The online version contains supplementary material available at https://doi.org/10.1038/s43018-023-00556-5.

Correspondence and requests for materials should be addressed to Hrvoje Miletic or Justin D. Lathia.

Peer review information *Nature Cancer* thanks Jonathan Brestoff, Luca Scorrano and Frank Winkler for their contribution to the peer review of this work.

Reprints and permissions information is available at www.nature.com/reprints.

Publisher's note Springer Nature remains neutral with regard to jurisdictional claims in published maps and institutional affiliations.

Dionysios C. Watson[1,2,3,4,22,23], Defne Bayik[1,2,22,23], Simon Storevik[5,6,23], Shannon Sherwin Moreino[5,23], Samuel A. Sprowls[1], Jianhua Han[5], Mina Thue Augustsson[5], Adam Lauko[1,7,8], Palavalasa Sravya[9], Gro Vatne Røsland[5], Katie Troike[1], Karl Johan Tronstad[5], Sabrina Wang[1], Katharina Sarnow[5], Kristen Kay[1], Taral R. Lunavat[5,10], Daniel J. Silver[1], Sahil Dayal[1], Justin Vareecal Joseph[11], Erin Mulkearns-Hubert[1,7], Lars Andreas Rømo Ystaas[5], Gauravi Deshpande[1], Joris Guyon[12], Yadi Zhou[1], Capucine R. Magaut[12], Juliana Seder[1], Laura Neises[13], Sarah E. Williford[14], Johannes Meiser[13], Andrew J. Scott[9,15], Peter Sajjakulnukit[16], Jason A. Mears[2,4], Rolf Bjerkvig[5,17], Abhishek Chakraborty[1,2], Thomas Daubon[18], Feixiong Cheng[1,2], Costas A. Lyssiotis[15,19,20], Daniel R. Wahl[9,15], Anita B. Hjelmeland[14], Jubayer A. Hossain[5], Hrvoje Miletic[5,21,24] ✉ & Justin D. Lathia[1,2,7,24] ✉

[1]Lerner Research Institute, Cleveland Clinic, Cleveland, OH, USA. [2]Case Comprehensive Cancer Center, Cleveland, OH, USA. [3]University Hospitals Cleveland Medical Center, Cleveland, OH, USA. [4]School of Medicine, Case Western Reserve University, Cleveland, OH, USA. [5]Department of Biomedicine, University of Bergen, Bergen, Norway. [6]Department of Neurology, Haukeland University Hospital, Bergen, Norway. [7]Cleveland Clinic Lerner College of Medicine, Case Western Reserve University, Cleveland, OH, USA. [8]Medical Scientist Training Program, Case Western Reserve University, Cleveland, OH, USA. [9]Department of Radiation Oncology, University of Michigan, Ann Arbor, MI, USA. [10]Department of Neurology, Molecular Neurogenetics Unit-West, Massachusetts General Hospital, Boston, MA, USA. [11]Stipe Therapeutics, Aarhus, Denmark. [12]University of Bordeaux, INSERM, BRIC, Pessac, France. [13]Cancer Metabolism Group, Department of Cancer Research, Luxembourg Institute of Health, Luxembourg, Luxembourg. [14]University of Alabama at

Birmingham, Birmingham, AL, USA. [15]Rogel Cancer Center, University of Michigan, Ann Arbor, MI, USA. [16]Cancer Biology Graduate Program, University of Michigan, Ann Arbor, MI, USA. [17]NorLux Neuro-Oncology Laboratory, Department of Cancer Research, Luxembourg Institute of Health, Luxembourg, Luxembourg. [18]University of Bordeaux, CNRS, IBGC, Bordeaux, France. [19]Department of Molecular & Integrative Physiology, University of Michigan, Ann Arbor, MI, USA. [20]Department of Internal Medicine, Division of Gastroenterology and Hepatology, University of Michigan, Ann Arbor, MI, USA. [21]Department of Pathology, Haukeland University Hospital, Bergen, Norway. [22]Present address: Sylvester Comprehensive Cancer Center, Miller School of Medicine, University of Miami, Miami, FL, USA. [23]These authors contributed equally: Dionysios C. Watson, Defne Bayik, Simon Storevik, Shannon Sherwin Moreino. [24]These authors jointly supervised this work: Hrvoje Miletic, Justin D. Lathia. ✉e-mail: hrvoje.miletic@uib.no; lathiaj@ccf.org

https://doi.org/10.1038/s43018-023-00556-5

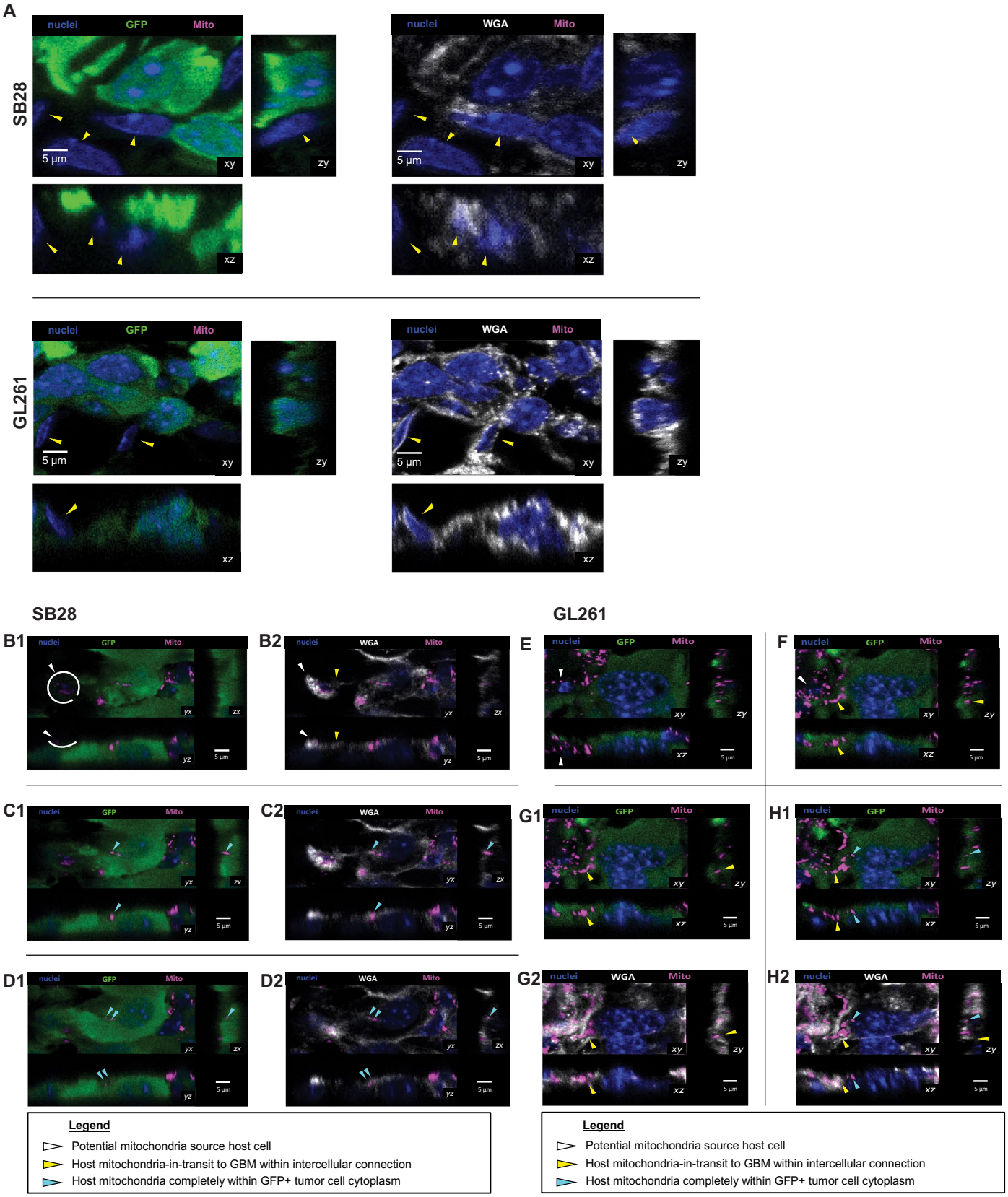

Extended Data Fig. 1 | See next page for caption.

https://doi.org/10.1038/s43018-023-00556-5

Extended Data Fig. 1 | Additional data for *in vivo* transfer of host mitochondria to orthotopic mouse GBM tumors. (**A**) GFP-expressing GL261 and SB28 mouse GBM cells were implanted intracranially into wildtype mice (controls for Fig. 1B-F), and tumors were analyzed at animal humane endpoint. Representative confocal microscopy data from orthotopic SB28 and GL261 tumors in wildtype mice are shown. Yellow arrowheads point to $GFP^{negative}$ (non-tumor) host cells. Shown are single focal planes (xy), as well as z-stacks (zy and xz). (**B**→**D**) and (**E**→**H**) Mitochondria in-transit from host to GBM cells in orthotopic tumors. Sequential confocal planes (xy) and accompanying orthogonal reconstructions (zy, xz) of SB28 (**B**→**D**) and GL261 (**E**→**H**) GBM tumors in mice, demonstrating an intercellular connection between a mito::$mKate2^+$ host cell (white arrowheads) and GFP^+ tumor cell. Host $mKate2^+$ mitochondria within the intercellular connection are indicated by yellow arrowheads. The mitochondria at the end of the connection are surrounded by GFP signal, corresponding to incorporation in the recipient tumor cell cytoplasm (cyan arrowhead).

https://doi.org/10.1038/s43018-023-00556-5

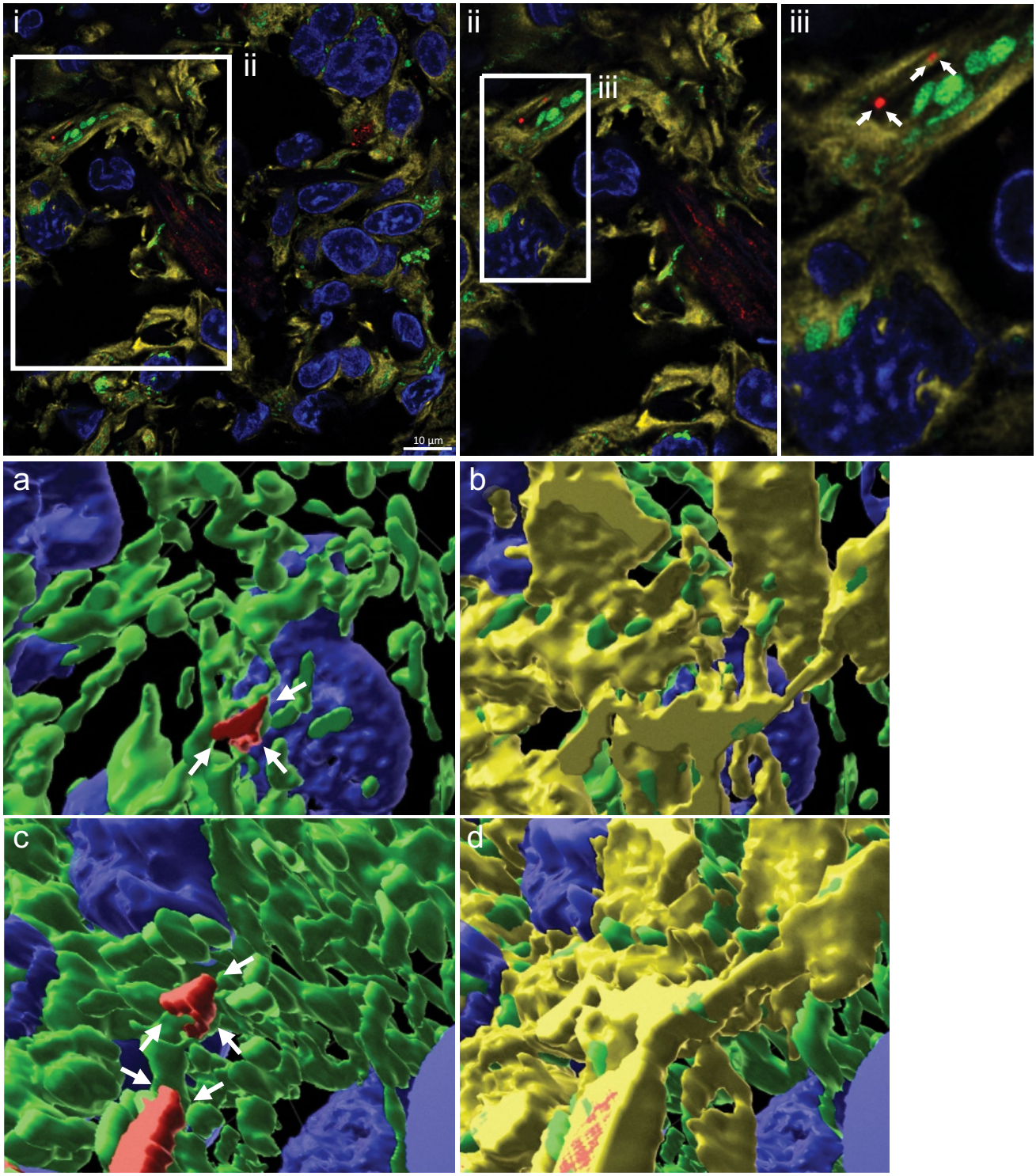

Extended Data Fig. 2 | Mitochondria transfer from the TME to human GBM models is observed *in vivo*. Mitochondria transfer between the TME (mitoDsRed +) and tumor cells (mitoGFP+ and nestin +) *in vivo*. Confocal microscopy of GG16 tumors immunostained with human-specific nestin antibodies, representative of at least four 100X images across 3 biologically independent animals. (i). Details of area along the tumor surface with co-localization of nestin + (yellow), mitoGFP+ and mitoDsRed+ signal (ii and iii). 3D reconstruction of the mitoDsRed+ mitochondria seen from above, without (a) and with (b) the nestin+ cell borders. From below, the mitoDsRed+ mitochondria are also visible (c) and reside within the cell (d). ii, 1.5x magnification; iii and a-d, 3x magnification.

https://doi.org/10.1038/s43018-023-00556-5

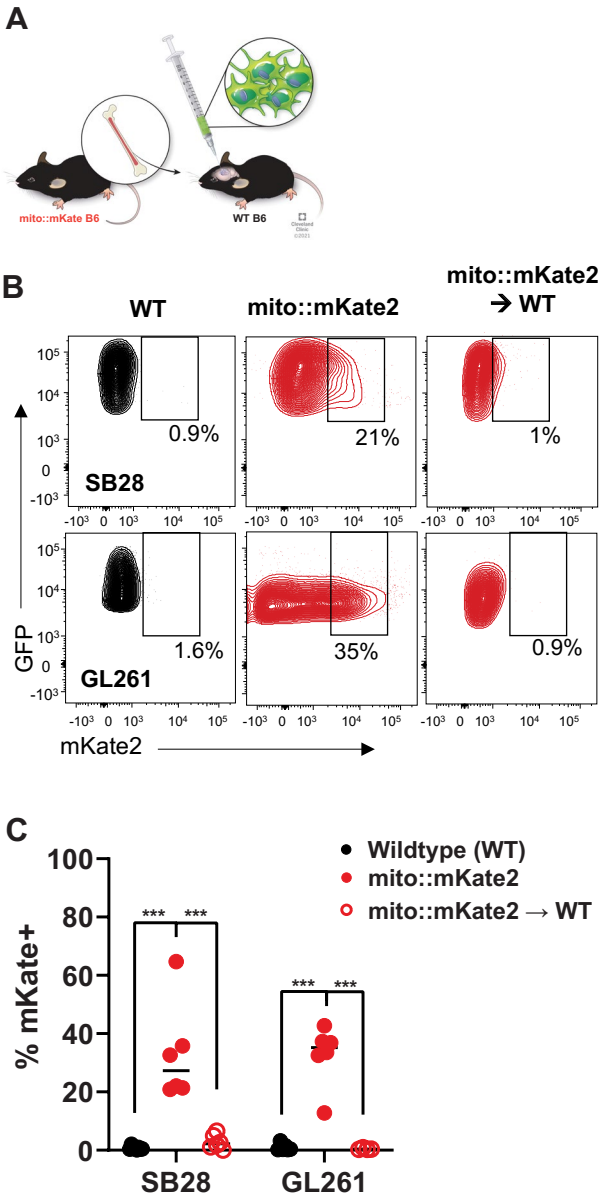

Extended Data Fig. 3 | Brain-resident cells transfer mitochondria to GBM cells *in vivo*. (**A-C**) GFP-expressing SB28 and GL261 cells were implanted intracranially into wild-type (WT), mKate2::mito (mKate2) or WT mice with mito::mKate2 bone marrow (mito::mKate2→WT). (**B**) Representative contour plots and (**C**) aggregate data of relative frequency of mito::mKate2^{+}GFP^{+} GBM cells by flow cytometry; n = SB28 (8 WT, 6 mito::mKate2, and 6 mito::mKate2→WT) and GL261 (6 WT, 6 mito::mKate2, and 4 mito::mKate2→>WT) mice per group. *** $p < 0.0001$, 2-way ANOVA with Tukey correction for multiple comparisons. Mitochondria transfer rate is negligible in mito::mKate2→WT mice, in which brain-resident cells do not express mito::mKate2.

https://doi.org/10.1038/s43018-023-00556-5

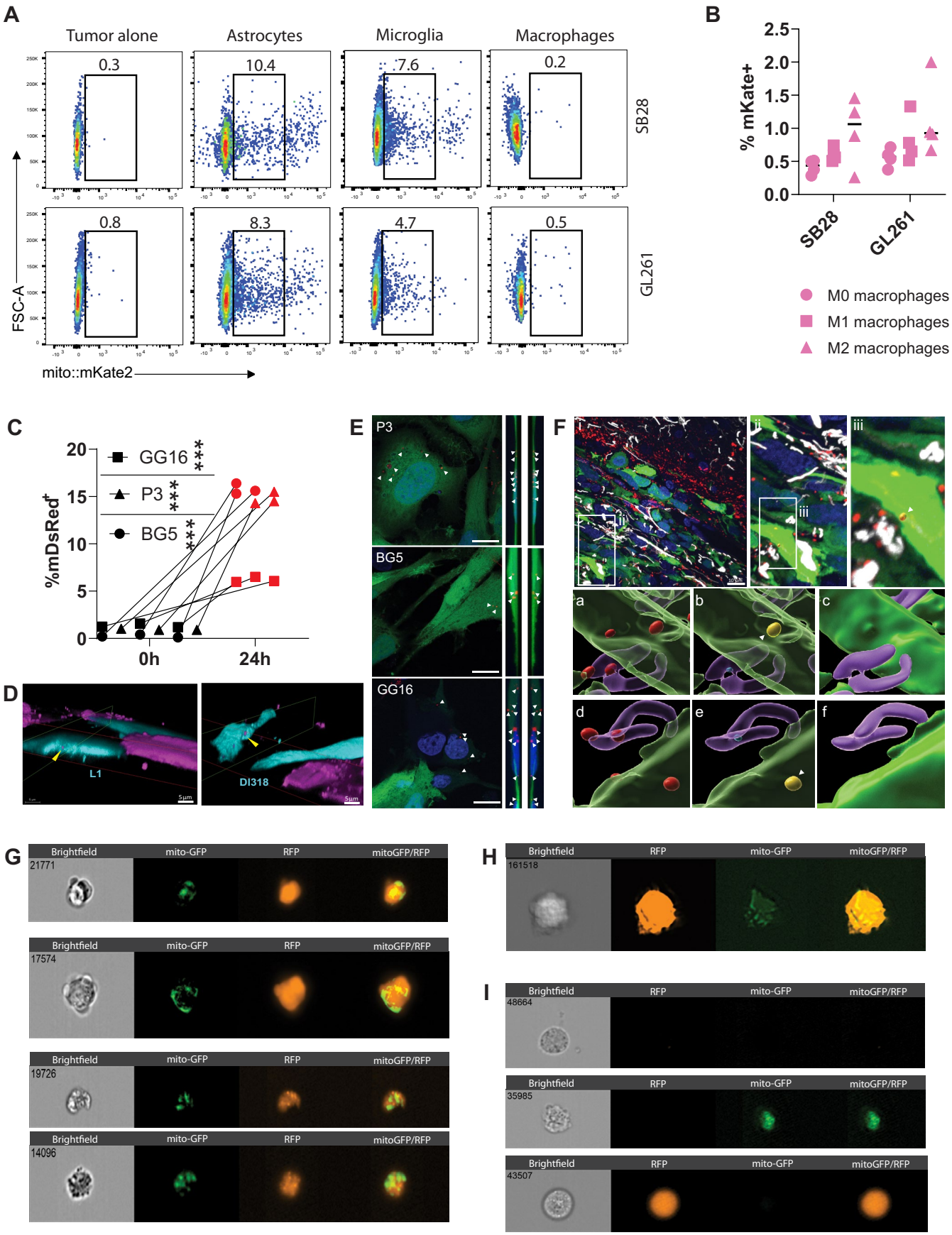

Extended Data Fig. 4 | See next page for caption.

https://doi.org/10.1038/s43018-023-00556-5

Extended Data Fig. 4 | Additional data for in vitro mitochondria transfer in mouse and diverse patient-derived GBM models. (**A**) Representative flow cytometry dot plots depicting mitochondria transfer frequency to mouse GBM cells from mito::mKate2 donor cells, summarized in Fig. 2B. (**B**) Mitochondria transfer from polarized (M1, M2) or non-polirized (M0) bone marrow-derived macrophages, assessed by flow cytometry. n = 4 independent experiments. Two-way ANOVA. (**C**) Flow cytometry of mitochondria transfer between mDsRed+ astrocytes and P3/BG5/GG16 GFP + cells at 24 h; mean ± SD. n = 3 independent experiments. *** $p < 0.0001$ (2-tailed t-test). (**D**) 3D reconstructions of confocal microscopy from patient-derived GBM and astrocyte co-cultures. mito-mCherry astrocytes (magenta); cyan cells CellTrace-labelled GSCs (cyan). Perpendicular cutaway planes (red and green outlines) reveal internalized astrocyte-derived mito-mCherry$^+$ mitochondria in GSCs (yellow arrowheads). (**E**) Confocal microscopy of mitochondria transfer in P3/BG5/GG16 GFP + cells with mDsRed+ astrocyte mitochondria (arrows); representative of at least four 100x images across 3 biologically independent animals for each cell line. Scale bars 10 mm. Z stack locates mDsRed+ mitochondria (arrows) within acceptor cell cytoplasm, from the left side (i) and the right (ii). **(F)** Mitochondria transfer between astrocytes (mitoDsRed$^+$GFAP$^+$) and human GBM cells (GFP$^+$) *in vivo*. Confocal microscopy of GFP$^+$ P3 xenograft tumor immunostained for GFAP (white) to visualize astrocytes; representative of at least six 100X images across 3 biologically independent animals. (i) Mitochondria transfer highlighted at invasive tumor area with colocalization of GFP + and mitoDsRed+ signal (ii and iii, higher magnification). 3D reconstruction of the mitoDsRed+ mitochondrial signal within and around GFP + and GFAP + surfaces (a). mitoDsRed+ mitochondria colocalize within GFP + tumor cells (yellow) and within the purple reconstructed GFAP + astrocytic processes (blue), seen from above without (b) and with (c) GFP + and GFAP + cell borders. From below, mitoDsRed+ mitochondria are also visible (d) and reside within the GFP + and GFAP + regions (e-f). Scale bars 10 µm. (**G-H**) ImageStream depicting transferred mito-GFP astrocyte mitochondria to co-cultured (**G**) D456 and (**H**) JX22 patient-derived RFP$^+$ GBM cells, representative across >imaged 100 cells per cell type and model. (**I**) Single-cell culture controls demonstrating the specificity of the RFP (tumor) and GFP (astrocyte mitochondria) signals. *Top to bottom:* Non-transduced GBM cells; mito-GFP astrocytes; RFP GBM cells.

https://doi.org/10.1038/s43018-023-00556-5

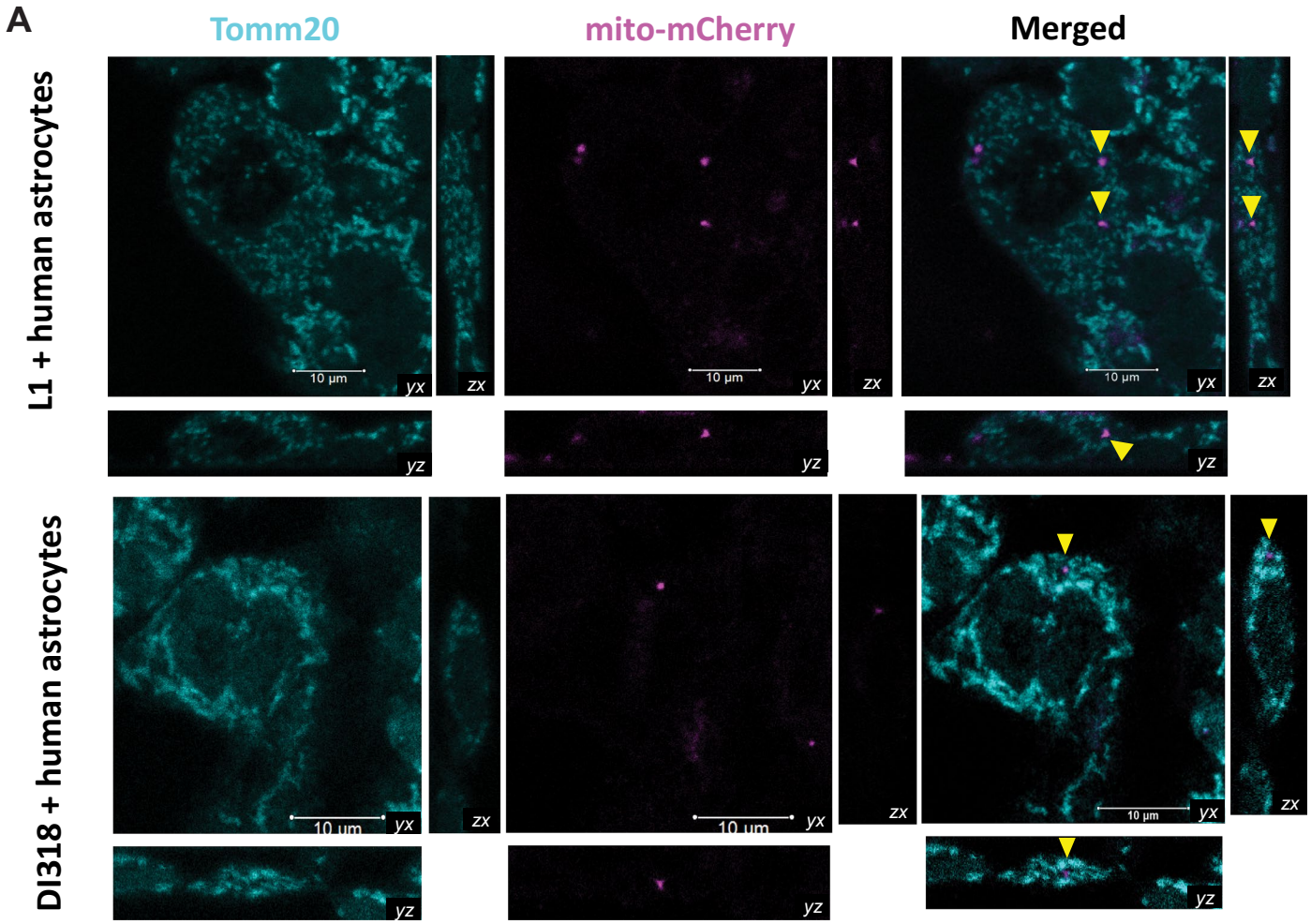

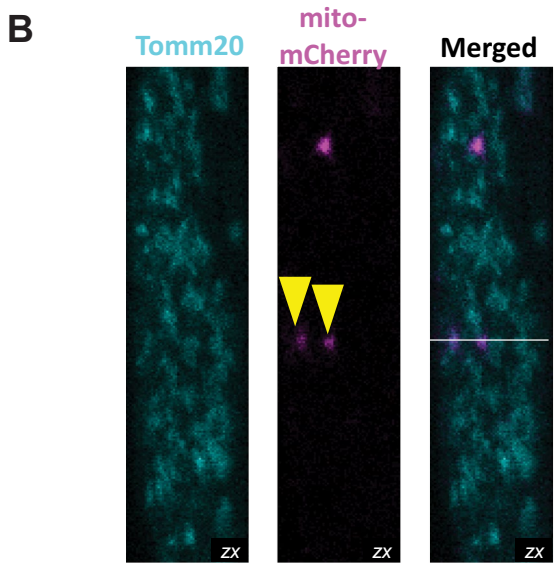

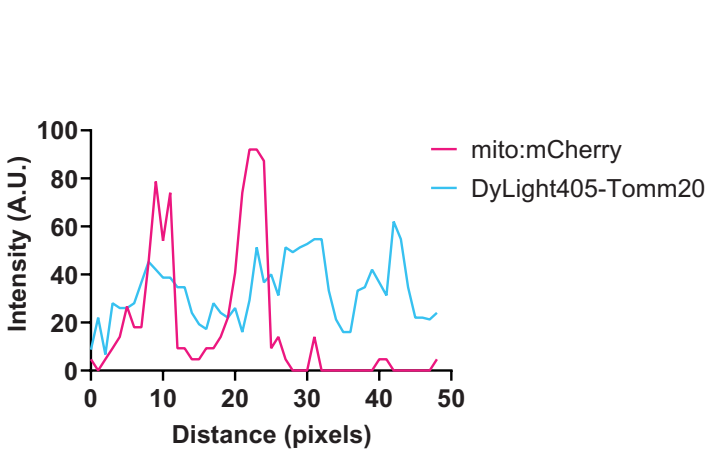

Extended Data Fig. 5 | Astrocyte mito-mCherry^{+} structures internalized by patient-derived GSCs comprise Tomm20^{+} mitochondria. Co-cultures of patient-derived GSCs (L1 and DI318) and mito-mCherry (magenta) human astrocytes were fixed and stained for the mitochondrial outer membrane protein Tomm20 (cyan). (**A**) Confocal microscopy, including z-stacks, depicting distribution of internalized astrocyte-derived mito-mCherry^{+} mitochondria (yellow arrowheads) in relation with intrinsic mCherry^{negative}Tomm20^{+} mitochondria in GSCs; representative of at least 3 different optical fields with evidence of mitochondria transfer, across 3 experiments (per model). Animation of the 3D reconstructions can be seen in Supplementary Videos 1-2. (**B**) Z-stacks of L1 cells with internalized astrocyte-derived mito-mCherry^{+} mitochondria (yellow arrowheads) were utilized to perform linear colocalization analysis of mito-mCherry with Tomm20 (analyzed pixels denoted with horizontal white line in the "merged" channel micrograph. (**C**) Linear colocalization analysis from **Panel B** data. Magenta mito-mCherry peaks coincide with cyan Tomm20 peaks, indicating colocalization.

https://doi.org/10.1038/s43018-023-00556-5

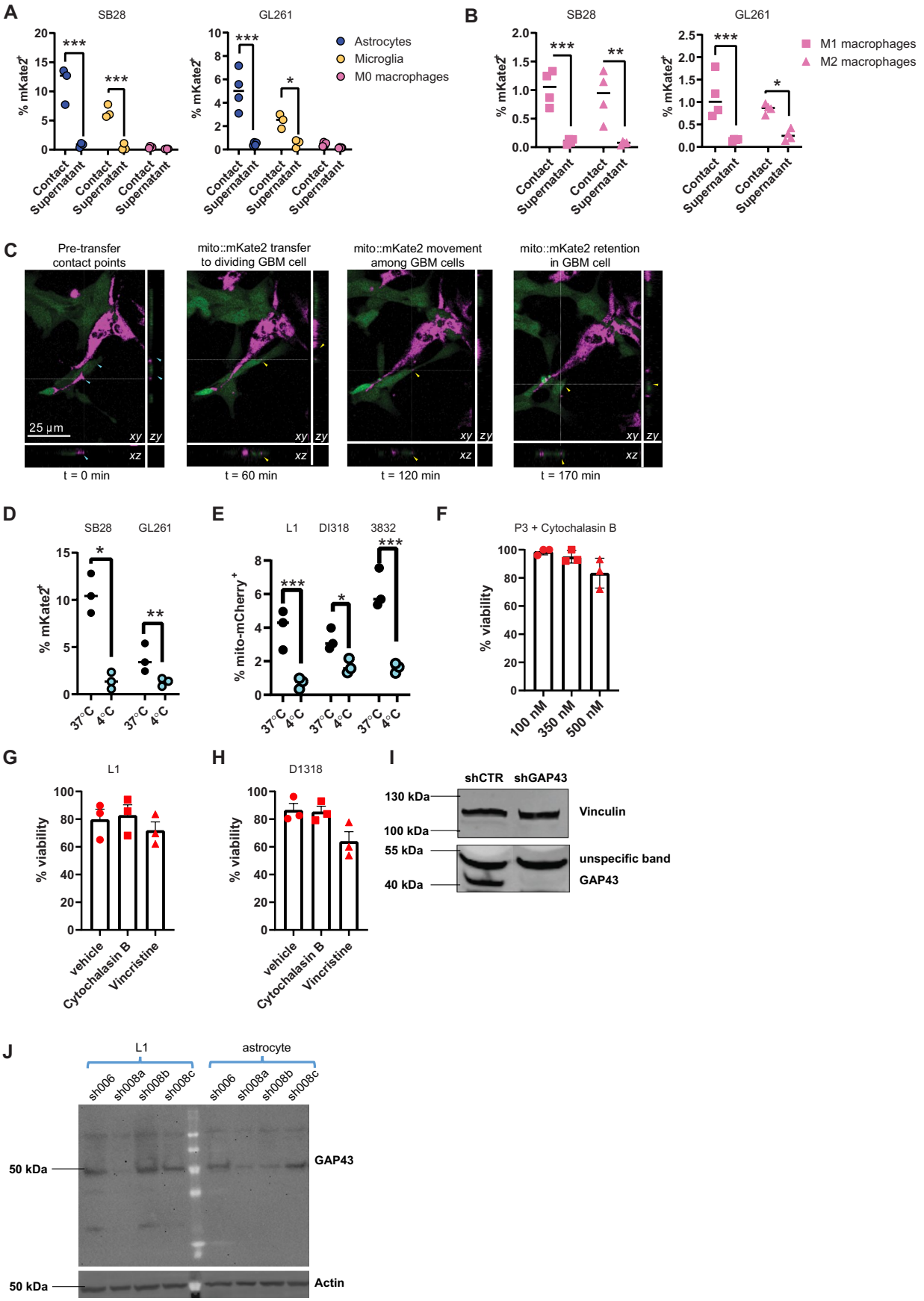

Extended Data Fig. 6 | See next page for caption.

https://doi.org/10.1038/s43018-023-00556-5

Extended Data Fig. 6 | Transfer of host mitochondria to GBM cells is contact-, energy-, actin-, and GAP43-dependent: additional data. (**A-B**) GBM cells were co-cultured in direct contact with astrocytes, microglia, or M0/M1/M2 macrophages from mito::mKate2 mice for 2 hours ("contact"). Alternatively, culture supernatant conditioned by donor cells for 48 hours was transferred to GBM cell cultures ("supernatant"). Mitochondria transfer was analyzed by flow cytometry. n = SB28 (3 astrocytes, 3 microglia, 4 macrophages, 4 M1 macrophages, 4 M2 macrophages and GL261 (4 astrocytes, 3 microglia, 4 macrophages, 4 M1 macrophages, 4 M2 macrophages) independent experiments. * p = 0.03 (GL261 microglia), 0.02 (GL261 M2 macrophages), ** p < 0.02, *** p = <0.0001 (astrocytes), 0.001 (SB28 microglia), 0.0007 (SB28 M1 macropahges), 0.0004 (GL261 M1 macrophages), two-way ANOVA. (**C**) Confocal time-lapse images demonstrating real-time acquisition of astrocyte mitochondria (magenta) by SB28 cells (green). Cyan arrowheads point to contact points between SB28 cells and astrocytes. Yellow arrowheads point to transferred mito-mCherry$^+$ astrocyte mitochondria inside SB28 cells. Video footage provided in Supplementary Video S3. (**D**) Mouse and (**E**) patient-derived GBM cells were co-cultured with mito::mKate2 or mito-mCherry (respectively) astrocytes for 2 hours at 37 °C or 4 °C. Graphs depict astrocyte mitochondria transfer to GBM cells. n = 3 independent experiments for each model. (**D**) * p = 0.04, ** p < 0.0003, (**E**) p = 0.0004 (L1), 0.03 (DI318), < 0.0001 (3832), two-way ANOVA with Sidak multiple comparison correction. (**F**) WST (viability) assay of P3 cells treated with cytochalasin B at indicated concentrations normalized to control. n = 3 independent experiments; mean ± SD. (**G-H**) Patient-derived GSCs were co-cultured for 24 h with mito-mCherry$^+$ human astrocytes in the presence of actin (cytochalasin B) or microtubule (vincristine) polymerization inhibitors or vehicle control. Viability of GSCs was assessed by flow cytometry. n = 3 independent experiments; mean ± SEM. * p < 0.05, ** p < 0.01, ANOVA. (**I**) Knockdown of GAP43 in P3 GBM cells. Western blot for GAP43 in shGAP43 and shCTR P3 cells, representative of 2 independent experiments. Vinculin was used as a loading control. (**J**) Western blot of patient-derived GSCs (L1) and immortalized mito-mCherry human astrocytes, confirming knockdown of GAP43 in cell cultures (once) prior to use for experiment series in Fig. 4D (L1-sh008a and astrocytes-sh008b).

https://doi.org/10.1038/s43018-023-00556-5

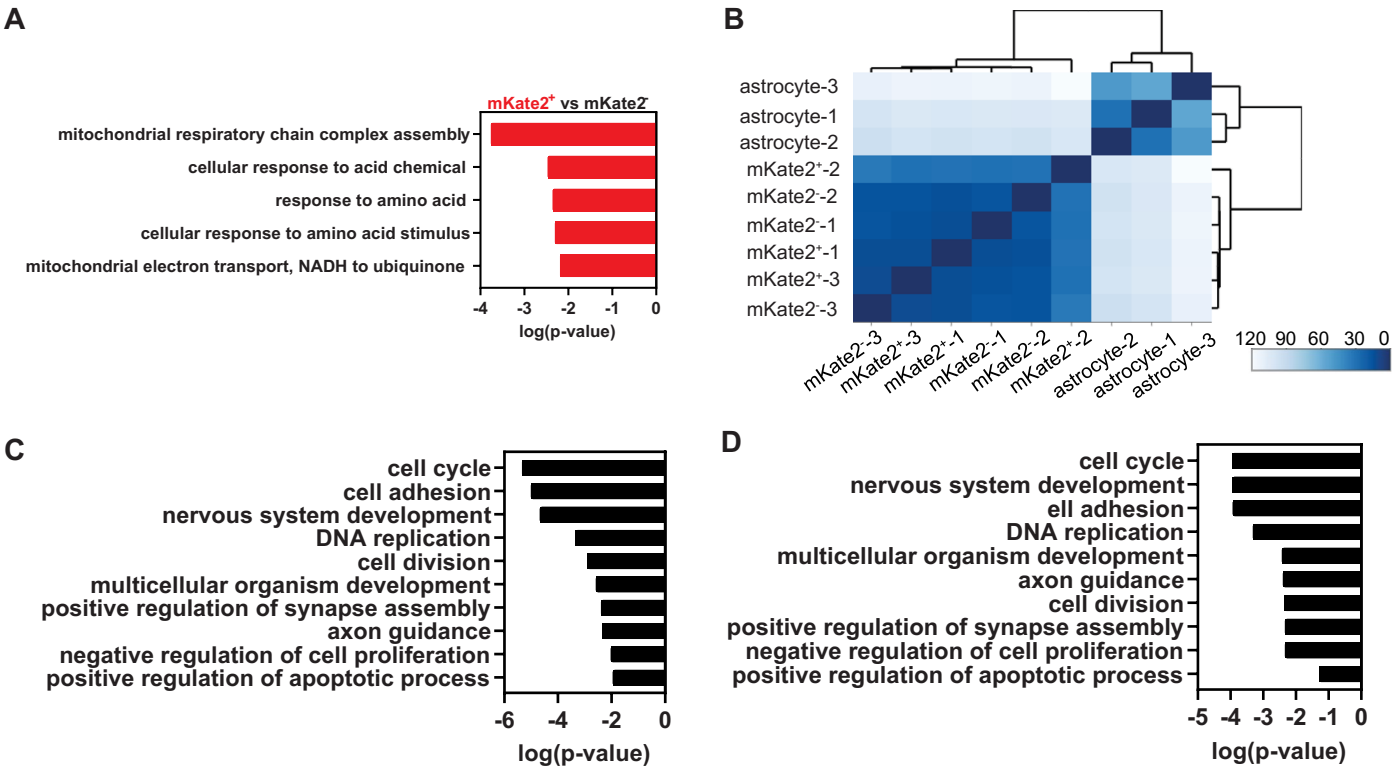

Extended Data Fig. 7 | Mitochondria transfer alters expression of metabolism gene pathways in recipient GBM cells. (**A-F**) RNAseq analysis from n = 3 independent co-culture experiments. (**A**) Top 5 pathways enriched in RNAseq data from sorted mKate2$^+$ versus mKate2$^-$SB28 cells based on genes upregulated >1.5 fold with p < 0.05 (one-tailed hypergeometric enrichment test, unadjusted p-values). (**B-D**) Data supporting purity of sorted cell populations in RNAseq experiments, given distinct transcriptomic signature of sorted astrocytes vs. GBM cells. (**B**) Heatmap demonstrating separate unsupervised hierarchical clustering of astrocytes from mKate2$^-$ and mKate2$^+$ tumor cells based on gene expression profiling. GO pathway analysis of differentially expressed genes between (**C**) mKate2$^-$ cells and astrocytes and (**D**) mKate2+ cells and astrocytes. One-tailed hypergeometric enrichment test, unadjusted p-values. (**E**) Volcano plot representing differential gene expression signature of mKate2$^+$ versus mKate2$^-$ cells. Dashed lines mark fold change > 1.5 and p-value < 0.05. Negative binomial distribution DESeq2 testing, unadjusted p-value. Genes that are mapped to mitochondria-related networks are shown in red. (**F**) Differentially up-regulated genes are enriched in the mitochondrial network. Protein-protein interaction network for the differentially expressed genes. Mouse genes were mapped to human genes according to NCBI HomoloGene. Protein-protein interactions were extracted for these genes/proteins using our human protein interactome. Diamond-shaped nodes indicate that these genes are mitochondrially localized based on the Human MitoCarta2.0 database. Node color shows the log2 fold change of the genes.

https://doi.org/10.1038/s43018-023-00556-5

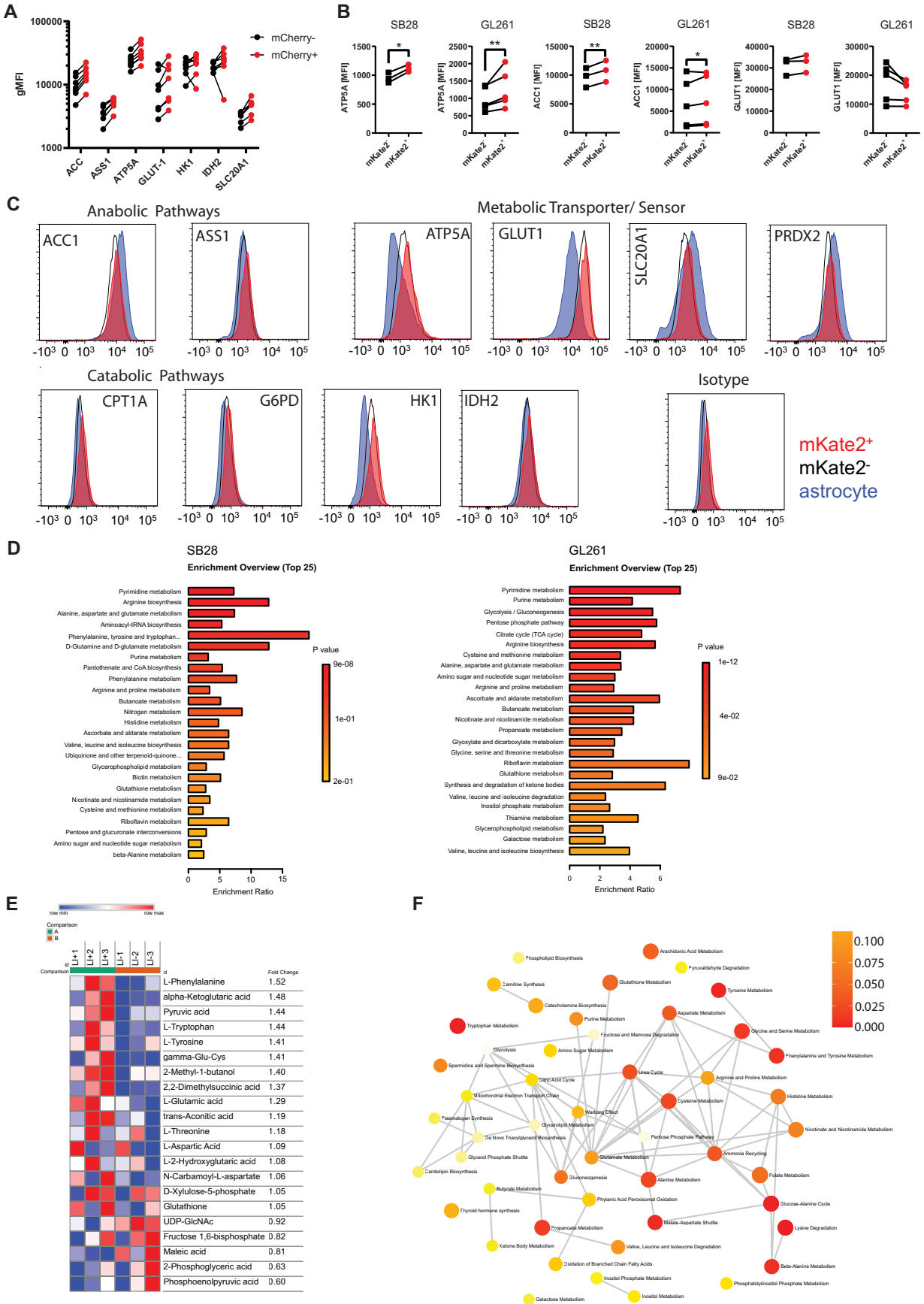

Extended Data Fig. 8 | See next page for caption.

https://doi.org/10.1038/s43018-023-00556-5

Extended Data Fig. 8 | Mitochondria transfer alters GBM metabolism at protein and metabolomic levels. (**A**) Aggregate data that is summarized in Fig. 5E. Graph depicts gMFI of metabolic protein expression assessed by flow cytometry in seven distinct patient-derived GSCs co-cultured with immortalized human mito-mCherry astrocytes for 4 days. Results of statistical analysis by mixed-effects model is summarized in Fig. 5E. (**B**) Mouse GBM cell lines were co-cultured with mito::mKate2^{+} astrocytes for 24 h and stained with antibodies against key metabolic proteins, as denoted. Expression levels were assessed by flow cytometry. Aggregate data from n = 3 (SB28) and 5 (GL261) independent experiments. Panels depict isotype background-corrected, geometric mean fluorescence intensity (gMFI) of the expression of the indicated metabolic proteins. * p = 0.02 (SB28), 0.03 (GL261), ** p = 0.004 (SB28), 0.009 (GL261), paired 2^{-}tailed t-test. (**C**) Representative histograms of data summarized in **Panel B**, depicting differential expression of critical metabolic proteins by astrocytes and mKate2^{+} and mKate2^{-} SB28 cells. Astrocytes had higher levels of acetyl-CoA carboxylase (ACC1), SLC20A1 and peroxiredoxin-2 (PRDX2), indicative of more oxidative phosphorylation. In contrast, tumor cells had higher levels of glucose transporter 1 (GLUT 1) and hexokinase 1 (HK1), pointing to a more glycolytic metabolism. (**D**) Mouse GBM cells were sorted from co-cultures with mouse mito::mKate2 astrocytes and analyzed by targeted metabolomics. Analysis depicts metabolic pathways upregulated in mito::mKate2^{+} vs. mito::mKate2^{-} GBM cells (MetaboAnalyst 5.0 one-tailed hypergeometric test; unadjusted p-values). This data was used in the combined analysis identifying mutually upregulated pathways in both models, shown in Fig. 6A. (**E**) L1 cells were co-cultured with immortalized human mito-mCherry astrocytes for 4 days and sorted for metabolite analysis. Heat map showing comparison of abundance of metabolites in mito-mCherry^{+} L1 cells (L1 +) when compared to mito-mCherry^{-} L1 cells (L1-). (**F**) Network of metabolites enriched more in mito-mCherry^{+} L1 cells when compared to mito-mCherry^{-} L1 cells (MetaboAnalyst 5.0 one-tailed hypergeometric test; unadjusted p-values).

https://doi.org/10.1038/s43018-023-00556-5

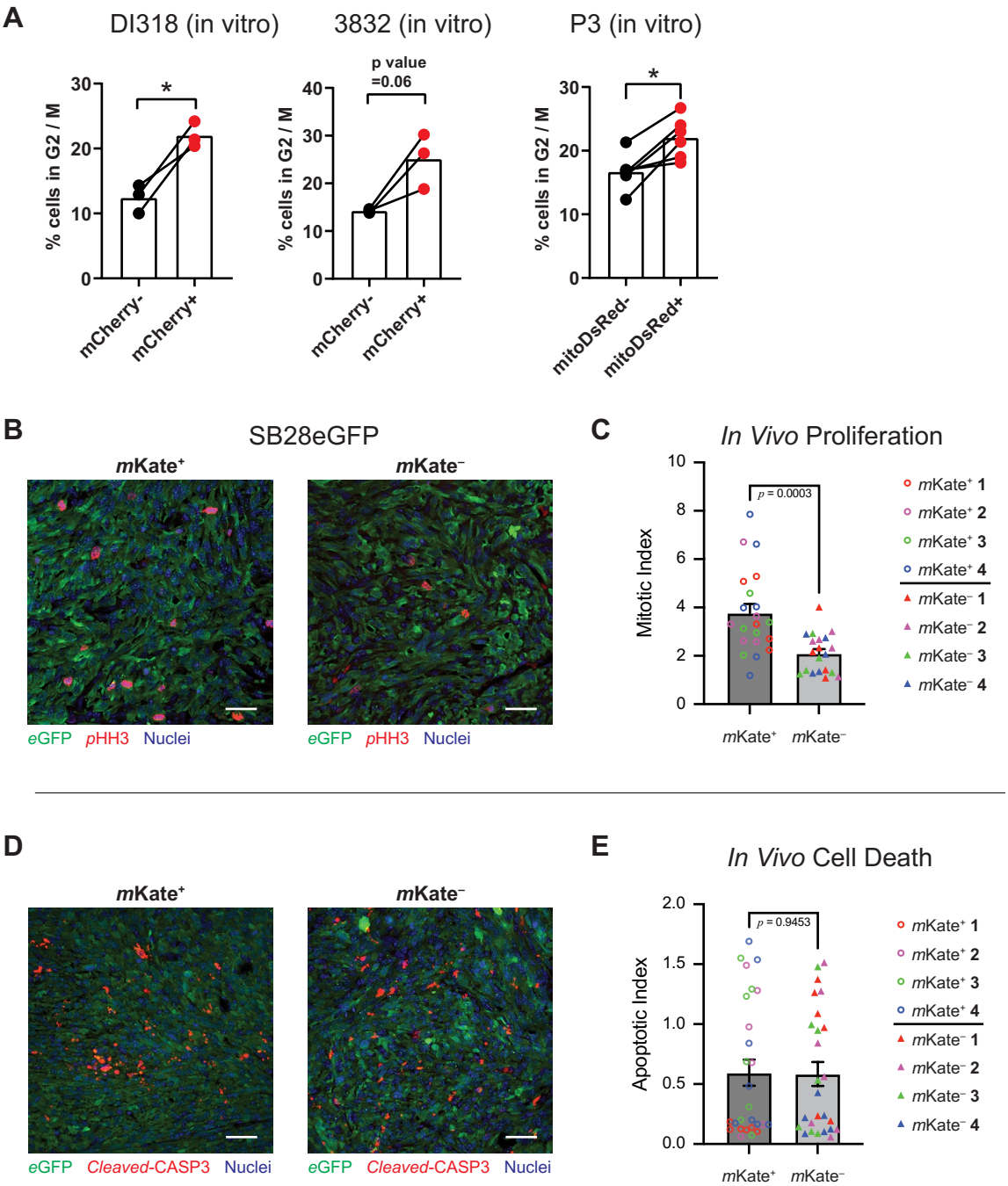

Extended Data Fig. 9 | GBM cells that acquire astrocyte mitochondria are more proliferative. (**A**) Three additional patient-derived GSC specimens were co-cultured with immortalized human mito-mCherry or mitoDsRed astrocytes for cell cycle analysis by flow cytometry DNA quantification. GBM cells that acquired astrocyte mitochondria (mCherry$^+$ or mitoDsRed$^+$) were more likely to be in G2/M phase. N = 3 (DI318), 3 (3832) and 6 (P3) biologically independent samples. * p = 0.04 (DI318), 0.01 (P3), 2-tailed t-test. (**B-E**) mKate2+ and mKate2- SB28 cells were sorted from co-cultures with mito::mKate2 astrocytes and implanted orthotopically in C57BL/6 mice. At humane endpoint, animals were euthanized and their brains fixed for subsequent histologic analysis. (**B**) Representative micrographs and (**C**) aggregate data from n = 4 mice per group assessing tumor mitotic index by phospho-histone H3 (pHH3) staining. p = 0.0003. (**D**) Representative micrographs and (**E**) aggregate data from n = 4 mice per group assessing apoptotic cell death of GBM cells by cleaved caspase-3 (cleaved-CASP3) staining. p = 0.9. Scale bar denotes 25 µm. Mean ± SEM, 2-tailed t-test.

https://doi.org/10.1038/s43018-023-00556-5

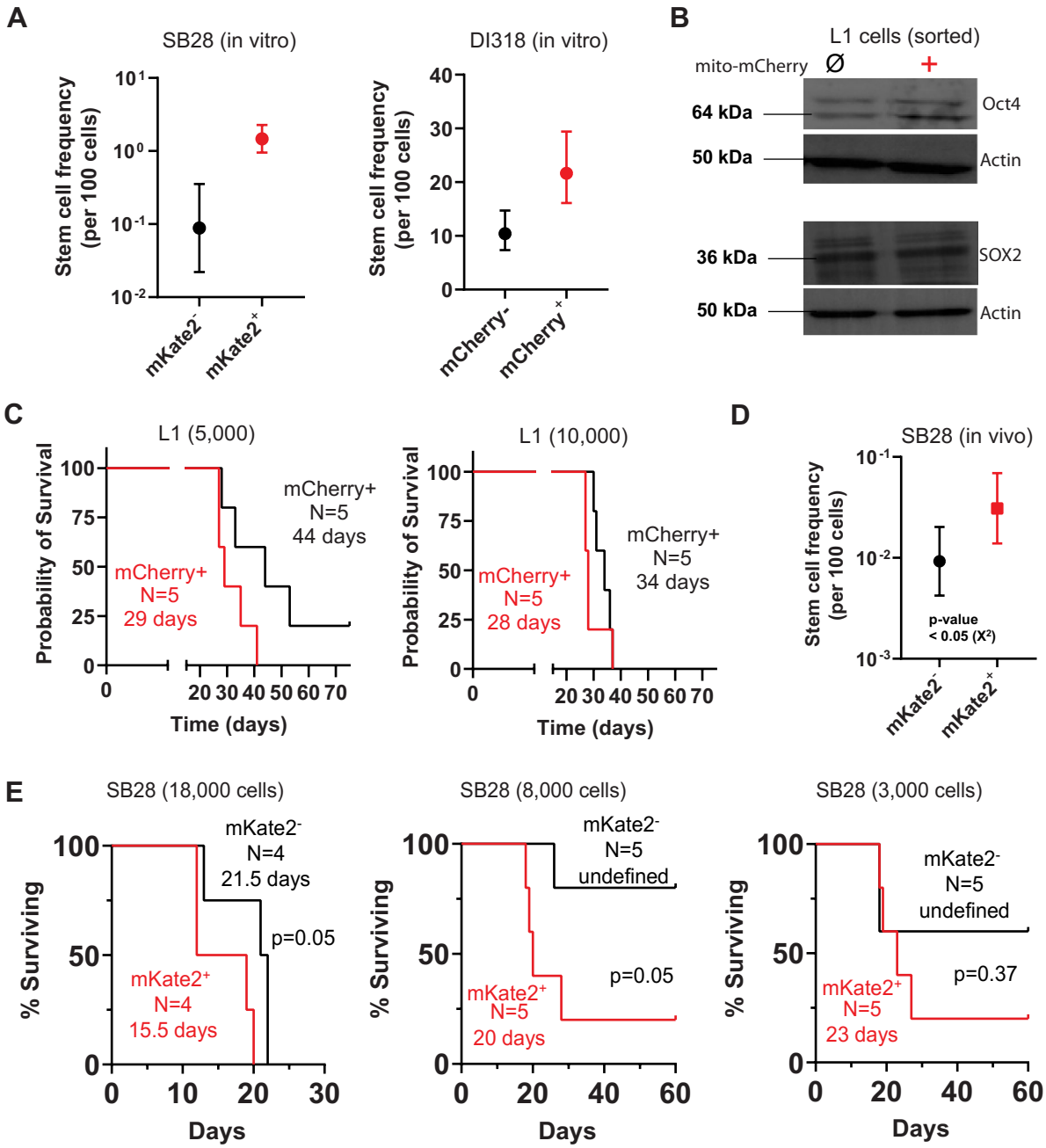

Extended Data Fig. 10 | Acquisition of astrocyte mitochondria enhances self-renewal and tumorigenicity in mouse and human models of disease. (**A**) Mouse GBM cells (SB28) and additional patient-derived GBM cells (DI318) were sorted from co-cultures and assayed for self-renewal by in vitro limiting-dilution sphere-formation assay. Representative experiments from 3 (SB28) and 2 (DI318) independent experiments are shown. Mean ± 95% confidence interval; analyzed by ELDA; p-value of individual experiments not shown. (**B**) mito-mCherry$^+$ and mito-mCherry$^-$ patient-derived GSCs (L1) sorted from one of the astrocyte co-cultures were analyzed by western blotting of stem cell transcription factors Oct4 and SOX2. (**C**) Additional survival curves of animals implanted with sorted L1 cells from co-cultures for the *in vivo* orthotopic tumor-initiation assay summarized in Fig. 7I. Log-rank test. (**D**) *In vivo* orthotopic tumor-initiation assay using mouse SB28 GBM cells sorted from mito::mKate2 astrocyte co-cultures. n = 14 mice per group (total 28 mice). Mean ± 95% confidence interval. p = 0.03, χ^2 test with 1 degree of freedom, analyzed by ELDA analysis. (**E**) Animal survival and tumor penetrance data at 3 different cell doses; used to calculate tumor initiating cell frequency in **Panel D**. Log-rank test.

nature portfolio

Corresponding author(s): Justin D. Lathia and Hrvoje Miletic

Last updated by author(s): Mar 2, 2023

Reporting Summary

Nature Portfolio wishes to improve the reproducibility of the work that we publish. This form provides structure for consistency and transparency in reporting. For further information on Nature Portfolio policies, see our Editorial Policies and the Editorial Policy Checklist.

Statistics

For all statistical analyses, confirm that the following items are present in the figure legend, table legend, main text, or Methods section.

n/a	Confirmed
☐	☒ The exact sample size (*n*) for each experimental group/condition, given as a discrete number and unit of measurement
☐	☒ A statement on whether measurements were taken from distinct samples or whether the same sample was measured repeatedly
☐	☒ The statistical test(s) used AND whether they are one- or two-sided *Only common tests should be described solely by name; describe more complex techniques in the Methods section.*
☒	☐ A description of all covariates tested
☐	☒ A description of any assumptions or corrections, such as tests of normality and adjustment for multiple comparisons
☐	☒ A full description of the statistical parameters including central tendency (e.g. means) or other basic estimates (e.g. regression coefficient) AND variation (e.g. standard deviation) or associated estimates of uncertainty (e.g. confidence intervals)
☐	☒ For null hypothesis testing, the test statistic (e.g. *F*, *t*, *r*) with confidence intervals, effect sizes, degrees of freedom and *P* value noted *Give P values as exact values whenever suitable.*
☒	☐ For Bayesian analysis, information on the choice of priors and Markov chain Monte Carlo settings
☒	☐ For hierarchical and complex designs, identification of the appropriate level for tests and full reporting of outcomes
☒	☐ Estimates of effect sizes (e.g. Cohen's *d*, Pearson's *r*), indicating how they were calculated

Our web collection on statistics for biologists contains articles on many of the points above.

Software and code

Policy information about availability of computer code

Data collection	BD LSR Fortessa/ BD FACS Symphony S6, FACS Diva v8.0 and v9.0 ; Agilent Seahorse Wave Controler v2.6.3, IDEAS software (version 6.2; EMD Millipore), LasX software (version 3.3, Leica and version LAS4.13), Fusion (Version 2020.2012.7), WorkOut (Version 2.0), LAS-3000 –(version 2.2)
Data analysis	FlowJo software (BD Biosciences, v10.7.2 or 10.8.1) was used to analyze flow cytometry data. ImageStream data was analyzed using IDEAS software (version 6.2; EMD Millipore). Image analyses were also performed with ImageJ (v2.3.0/1.53f) and Imaris (v9.6). Graphs were generated and statistical analysis were performed using Excel (Microsoft Office, v16.52), Prism (GraphPad, v9.1.0 or v9.2.0) or RStudio (v2022.02.1) software. ELDA tool (http://bioinf.wehi.edu.au/software/elda/) . LasX software (version 3.3, Leica). Velocity software (version 6.3, PerkinElmer) After Illumina sequencing of universal adapters were trimmed, the reads were mapped to the Mus musculus GRCm38 reference genome using the STAR aligner v.2.5.2b. Unique gene hit counts were calculated by using featureCounts from the Subread package v.1.5.2. Differential expression analysis was performed using edgeR 3.34. The mouse differentially expressed genes (DEGs) were mapped to the human homologs using the NCBI HomoloGene database (https://www.ncbi.nlm.nih.gov/homologene). We then performed the enrichment analysis using Enrichr for the entire DEGs and for the up- and down-regulated genes separately. The protein-protein interactions (PPIs) among the DEGs were extracted using a human protein interactome we built previously (citation in main text) that contains 17,706 protein nodes and 351,444 PPI edges. We then visualized this protein-protein interaction network using Cytoscape 3.8. Genes that localize to mitochondria are indicated by diamond node shape based on the Human MitoCarta2.0 database. Mouse metabolomics: Data were normalized by peak count. Values of zero (below limit of quantitation) were substituted with the approximate limit of quantitation (2000 peak count) to facilitate fold-change analysis. Metabolites enriched by >20% in mKate2+ GBM cells

were put into the metabolic pathway enrichment analysis algorithm MetaboAnalyst 5.0 web tool (www.metaboanalyst.ca) . Settings for analysis were as follows: HMDB and KEGG compound names; feature type = metabolites; KEGG analysis.

Human metabolomics: Agilent MassHunter Workstation Quantitative Analysis for QQQ Version 10.1, Build 10.1.733.0 was used to integrate and quantitate metabolite peak areas. LC-MS peaks corresponding to metabolites with coefficients of variation greater than 0.5 underwent manual inspection and integration. The data was normalized to the average sum of metabolites from all the samples and analyzed using Morpheus to generate the heatmap, Metaboanalyst to compare metabolites and metabolic pathways enriched in mito-mCherry+ L1 cells and mito-mCherry- L1 cells.

Phospho-array: Analysis was conducted using the phosphorylation ratio of each protein for samples tested (phosphorylated protein signal divided by corresponding total protein signal). We analyzed the functional enrichment of the upregulated phosphoproteins using Enrichr against the Gene Ontology (GO) biological process term data set. GO terms with FDR < 0.05 were considered significantly enriched. We summarized the enriched terms using Revigo to generate a graph-based view of the subdivisions of the terms.

Citations for all analysis software algorithms used are provided in the manuscript.

Summary list of all software used:
FACS Diva v8.0 and v9.0
Agilent Seahorse Wave Controler v2.6.3
IDEAS software (version 6.2; EMD Millipore)
LasX software (version 3.3, Leica and version LAS4.13),
LAS-3000 –(version 2.2, Fujifilm)
Velocity software (version 6.3, PerkinElmer)
FlowJo software (BD Biosciences, v10.7.2 or 10.8.1)
ImagePro Plus 10 (Media Cybernetics)
ImageJ (v2.3.0/1.53f)
Imaris v9.6 (Oxford Instruments)
ELDA (October 24, 2014 version)
Agilent MassHunter Workstation Software LC/MS Data Acquisition for 6400 Series Triple Quadrupole MS with Version B.08.02
Agilent MassHunter Workstation Quantitative Analysis for QQQ Version 10.1, Build 10.1.733.0
Morpheus (Broad Institute; https://software.broadinstitute.org/morpheus/)
Revigo (http://revigo.irb.hr/)
STAR aligner v.2.5.2b
Subread package v.1.5.2
DESeq2 (no version number)
Enrichr (no version number)
edgeR 3.34
Cytoscape 3.8
Graphpad Prism 8.2.1 and 9.2.0
Microsoft Excel v16.52

For manuscripts utilizing custom algorithms or software that are central to the research but not yet described in published literature, software must be made available to editors and reviewers. We strongly encourage code deposition in a community repository (e.g. GitHub). See the Nature Portfolio guidelines for submitting code & software for further information.

Data

Policy information about availability of data

All manuscripts must include a data availability statement. This statement should provide the following information, where applicable:

- Accession codes, unique identifiers, or web links for publicly available datasets
- A description of any restrictions on data availability
- For clinical datasets or third party data, please ensure that the statement adheres to our policy

Sequencing files have been deposited to GEO with the accession number GSE183004. Metabolic pathway analysis was based on the KEGG human metabolic pathways database (Oct. 2019) (https://www.genome.jp/kegg/pathway.html#metabolism). Protein phospho array data was mapped to pathways based on the Gene Ontology (GO) biological process term data set (http://geneontology.org/). RNAseq reads of mouse cells were mapped to the Mus musculus GRCm38 reference genome (https://www.ncbi.nlm.nih.gov/assembly/GCF_000001635.20/). RNAseq inferred protein-protein interaction network was constructed by mapping to human homologs using the NCBI HomoloGene database (https://www.ncbi.nlm.nih.gov/homologene). Genes encoding mitochondria localizing proteins were identified with Mitocarta 2.0 (https://www.broadinstitute.org/files/shared/metabolism/mitocarta/human.mitocarta2.0.html). All other data are available in the manuscript and supplementary materials.

Human research participants

Policy information about studies involving human research participants and Sex and Gender in Research.

Reporting on sex and gender	Not applicable. De-identified patient-derived cell models were used.
Population characteristics	Not applicable
Recruitment	Not applicable
Ethics oversight	Patient material was obtained from surgeries performed at the Haukeland University Hospital (Bergen, Norway). Written

Ethics oversight	consent was obtained from patients with procedures that were approved for the projects (project numbers 013.09 and 151825) by the Regional Ethical Committee (Bergen, Norway). Animal experiments were approved by the Institutional Animal Care and Use Committee of Cleveland Clinic and local ethical committee (Bergen, Norway). Animals were treated in accordance with the Norwegian Animal Act.

Note that full information on the approval of the study protocol must also be provided in the manuscript.

Field-specific reporting

Please select the one below that is the best fit for your research. If you are not sure, read the appropriate sections before making your selection.

☒ Life sciences ☐ Behavioural & social sciences ☐ Ecological, evolutionary & environmental sciences

For a reference copy of the document with all sections, see nature.com/documents/nr-reporting-summary-flat.pdf

Life sciences study design

All studies must disclose on these points even when the disclosure is negative.

Sample size	For most in vitro experiments, a minimum of 3 independent samples was used per experimental group. This gave sufficient power to detect differences among groups with large magnitude of effects. The minimum sample size for RNAseq was limited to 3 due to practical considerations associated with labor, time and cost of sample generation and analysis. As indicated in the manuscript, this allowed only for hypothesis generation using differentially expressed genes detected by statistical comparisons without multiple comparison correction. For metabolic flow analysis, sample size was increased to 5-6 per group, as the expected difference in metabolic protein expression was smaller. For phospho-array, 3 independent biological samples were analyzed via pooled assay. for metabolomics analysis, 3 biological replicates were analyzed independently. For in vivo experiments, sample size was determined based on minimum utilization of vertebrate animals and high expected magnitude of effect.
Data exclusions	no data were excluded from analyses
Replication	Experiments were conducted across time, with primary cells derived from multiple animals, different cell passages/vials (cell lines), by >1 researcher. Findings were replicated across multiple models of GBM, and accross species (mouse, rat, human). Key findings were replicated across institutions by independent research teams (primarily Cleveland Clinic and University of Bergen). Metabolomics were conducted in two separate facilities for each of the mouse and human assays. In vivo experiments were replicated with multiple models (mouse, human). Findings were reproducible under these conditions.
Randomization	Mice were randomized prior to tumor implantation. Rats were not randomized as only one experimental group was used to show mitochondrial transfer in vivo. For in vitro data, randomization is not relevant as specific cell lines were used.
Blinding	For all survival studies, researchers were blinded to the group assignment of mice with intracranial tumors. In vitro experiments were performed by one person/experiment, so blinding was not possible.

Reporting for specific materials, systems and methods

We require information from authors about some types of materials, experimental systems and methods used in many studies. Here, indicate whether each material, system or method listed is relevant to your study. If you are not sure if a list item applies to your research, read the appropriate section before selecting a response.

Materials & experimental systems

n/a	Involved in the study
☐	☒ Antibodies
☐	☒ Eukaryotic cell lines
☒	☐ Palaeontology and archaeology
☐	☒ Animals and other organisms
☒	☐ Clinical data
☒	☐ Dual use research of concern

Methods

n/a	Involved in the study
☒	☐ ChIP-seq
☐	☒ Flow cytometry
☒	☐ MRI-based neuroimaging

Antibodies

Antibodies used	Antibody / Supplier / Clone / Cat. No / Lot no. / Dilution factor used 1 . chicken anti-GFP antibody / AvesLabs / AB_2307313 / GFP-1020 / GFP3717982 / 1000 2 . donkey anti-chicken AF488 / Jackson ImmunoResearch / AB_2340375 / 703-545-155 / 162189 / 500 3 . APC-conjugated anti-CD11b antibody / Biolegend / M1/70 / 101212 / B288782 / 100 4 . ASS1 / Abcam / 2B10 / ab124465 / GR3209494-9 / 200 5 . anti-ATP synthase F1 subunit alpha (ATP5A) / Abcam / 7H10BD4F9 / ab110273 / GR3242541-11 / 1000

6 . anti-glucose transporter 1 (GLUT1) / Abcam / EPR3915 / ab115730 / GR3266142-11 / 40
7 . anti-glucose 6 phosphate dehydrogenase (G6PD) / Abcam / EPR20668 / ab210702 / GR3218248 / 400
8 . anti-Acetyl-CoA carboxylase (ACC1) / Abcam / EPR23235-147 / ab269273 / GR3340965-3 / 1000
9 . anti-peroxiredoxin 2 (PRDX2) / Abcam / EPR5154 / ab109367 / GR3257260-4 / 200
10 . anti-hexokinase 1 (HK1) / Abcam / EPR10134(B) / ab150423 / GR105890-12 / 20
11 . anti-Carnitine palmitoyltransferase I (CPT1A) / Abcam / EPR21843-71-2F / ab234111 / GR3351270-6 / 20
12 . anti-mouse IgG1 kappa monoclonal / Abcam / MOPC21 / ab18443 / GR3364197-6 / 200
13 . anti-mouse IgG2b kappa monoclonal / Abcam / 7E10G10 / ab170192 / GR3364314-1 / 1000
14 . Rabbit IgG monoclonal / Abcam / EPR25A / ab172730 / GR3284310-21 / 20-50
15 . Goat Anti- Mouse IgG H&L (Alexa Fluor® 647) / Abcam / n/a / ab150119 / GR3348378-3 / 2000
16 . Donkey Anti-Rabbit IgG H&L (Alexa Fluor® 647) / Abcam / n/a / ab150075 / GR3372283-8 / 2000
17 . anti-isocitrate dehydrogenase 2 (IDH2) / Abcam / EPR7577 / ab131263 / GR93077-12 / 100
18 . anti-SLC20A1 / Thermo Fisher Scientific / n/a / 12423-1-AP / 6201 / 200
19 . human-specific anti-nestin / Sigma-Aldrich / 10C2 / MAB5326 / 3822810 / 200 (tissue sections); 300 (cell culture)
20 . TOMM20 / Abcam / / ab78547 / GR3406425-1 and GR244837-3 / 400
21 . GAP43 / Abcam / EP890Y / ab75810 / GR42490-38 / 1000
22 . GFAP / Invitrogen / GA5 / 14-9892-82 / 2358413 / 200
23 . Vinculin / Invitrogen / VLN01 / MA511690 / VI3084704 / 2000
24 . F - Actin / abcam / 4E3.adl / ab130935 / GR3374194-6 / 5 mcg/mL
25 . goat-anti-mouse 647 / ThermoFisher / AB_2535804 / A-21235 / 2482945 / 200
26 . goat-anti-mouse 488 / Abcam / n/a / ab150117 / 814801 / 400
27 . goat-anti-rabbit 647 / ThermoFisher / n/a / A-21245 / 1910774 and 2299231 / 200 (tissue sections); 500 (cell culture)
28 . goat-anti-mouse HRP / Invitrogen / polyclonal / #31430 / ZC1230 / 10000
29 . goat-anti-rabbit HRP / Invitrogen / polyclonal / #31462 / 814801 / 10000
30 . rabbit-anti-phopho-histone H3 (Ser10) / Cell Signaling Technology / polyclonal / #9701 / no. 17 / 1000
31 . rabbit-anti-cleaved caspase-3 (Asp175) / Cell Signaling Technology / polyclonal / #9661 / #47 / 1000
32 . Tomm20 (for L1 and Di318 model assays) / Cell Signaling Technology / D8T4N / 42406 / no. 4 / 200
33 . anti-rabbit DyLight405 alpaca antibody / Jackson ImmunoResearch / AB_2922864 / 611-474-215 / / 300
34 . anti-actin hFAB Rhodamine / Bio-Rad / n/a / #12004163 / 64422460 / 5000
35 . anti-sox2 / R&D Systems / 245610 / MAB2018 / KGQ0319101 / 1000
36 . anti-oct4 / Cell Signaling Technology / polyclonal / #2750 / no. 5 / 1000
37 . ATP5A-AF647 / Abcam / EPR13030(B) / ab176569 / gr3399307-3 / 50
38 . GLUT1-AF647 / Abcam / EPR3915 / ab115730 / gr3406572-2 / 500

Validation

Antibody / Supplier / Cat. No / Validation
1 . chicken anti-GFP antibody / AvesLabs / GFP-1020 / Manufacturer COA detected GFP in transgenic mice (Western and microscopy)
2 . donkey anti-chicken AF488 / Jackson ImmunoResearch / 703-545-155 / Manufacturer COA reports minimal cross reactivity with non-chicken serum proteins
3 . APC-conjugated anti-CD11b antibody / Biolegend / 101212 / Manufacturer COA with appropriate staining of CD11b positive cells in mixed cel population of mouse bone marrow cells
4 . ASS1 / Abcam / ab124465 / Manufacturer COA reports appropriate band size detection by western blot across multiple cell types
5 . anti-ATP synthase F1 subunit alpha (ATP5A) / Abcam / ab110273 / Manufacturer COA reports appropriate size protein detection by western blot human/mouse cells; and appropriate localization to mitochondria on microscopy
6 . anti-glucose transporter 1 (GLUT1) / Abcam / ab115730 / Manufacturer COA reports specific binding across multiple cell lines, and no binding in knockout cells
7 . anti-glucose 6 phosphate dehydrogenase (G6PD) / Abcam / ab210702 / Manufacturer COA reports detection of appropriately sized protein on Western, and detection in appropriate cell types on histologic analysis of multiple organs
8 . anti-Acetyl-CoA carboxylase (ACC1) / Abcam / ab269273 / Manufacturer COA reports appropriate protein size detectoin by western, including for mouse and human cells, with variation of expression levels of target. Histologic analysis with appropriate cell labeling
9 . anti-peroxiredoxin 2 (PRDX2) / Abcam / ab109367 / Manufacturer COA reports appropriate band size and histologic staining across mouse and human samples. Loss of detection in target knockout cells
10 . anti-hexokinase 1 (HK1) / Abcam / ab150423 / Manufacturer COA reports appropriate band size and histologic staining across mouse and human samples. Loss of detection in target knockout cells
11 . anti-Carnitine palmitoyltransferase I (CPT1A) / Abcam / ab234111 / Manufacturer COA reports appropriate band size and histologic staining across mouse and human samples. Loss of detection in target knockout cells
12 . anti-mouse IgG1 kappa monoclonal / Abcam / ab18443 / Manufacturer COA reports lack of binding to broad array of human and mouse cell and tissue lysates
13 . anti-mouse IgG2b kappa monoclonal / Abcam / ab170192 / Manufacturer COA reports lack of binding to broad array of human and mouse cell and tissue lysates
14 . Rabbit IgG monoclonal / Abcam / ab172730 / Manufacturer COA reports lack of binding to broad array of human and mouse cell and tissue lysates
15 . Goat Anti- Mouse IgG H&L (Alexa Fluor® 647) / Abcam / ab150119 / Manufacturer COA reports reacts specifically with mouse IgG and with light chains common to other mouse immunoglobulins. No antibody was detected against non-immunoglobulin serum proteins. Reduced cross-reactivity to bovine, chicken, horse, human, pig, rabbit and rat IgG was detected. This antibody may cross react with IgG from other species.
16 . Donkey Anti-Rabbit IgG H&L (Alexa Fluor® 647) / Abcam / ab150075 / Manufacturer Coa reports specific binding to rabbit IgG with minimal cross reactivity to other immunoglobulins
17 . anti-isocitrate dehydrogenase 2 (IDH2) / Abcam / ab131263 / Manufacturer COA reports appropriate band size and histologic staining across mouse and human samples. Loss of detection in target knockout cells
18 . anti-SLC20A1 / Thermo Fisher Scientific / 12423-1-AP / Manufacturer COA reports appropriate band size and histologic staining across mouse and human samples.
19 . human-specific anti-nestin / Sigma-Aldrich / MAB5326 / Manufacturer COA and PMID 17202146 show postive signal of appropriate MW in human cells epxressing nestin. Species specificity was validated in this manuscript using rodent vs. human tissue

20 . TOMM20 / Abcam / ab78547 / Manufacturer COA demonstrates appropriate size (Western blor) and localizatoin (microscopy) of staining. We also validated TOMM20 is localized in mitochondria which was verified by colocalization with mitoDsRed.
21 . GAP43 / Abcam / ab75810 / Manufacturer COA with detection of appropriate size protein (western) and tissue distribution (microscopy) of target protein in human, mouse, and rat samples
22 . GFAP / Invitrogen / 14-9892-82 / Manufacturer COA demonstrates tissue specific (present in brain, absent in liver) of rat and mouse.
23 . Vinculin / Invitrogen / MA511690 / Manufacturer COA with advanced validation using cell lines +/- expression of vinculin
24 . F - Actin / abcam / ab130935 / Manufacturer COA reports appropriate band size (western) and cell localization on microscopy. Mouse and human cell targets
25 . goat-anti-mouse 647 / ThermoFisher / A-21235 / Manufacturer COA demonstrates appropriate staining of mouse primary antibodies and low cross-reactivity with non mouse
26 . goat-anti-mouse 488 / Abcam / ab150117 / Manufacturer COA shows minimal cross-reactivity with non-rodent IgG and appropriate staining when using a mouse primary antibody
27 . goat-anti-rabbit 647 / ThermoFisher / A-21245 / Manufacturer COA demonstrates appropriate staining vs. isotype control, and loss of staining in knockout models for target of primary antibody used in experiments
28 . goat-anti-mouse HRP / Invitrogen / #31430 / Manufacturer COA reports specific binging to mouse IgG and not other serum proteins. Minimal cross-reactivity with non-mouse IgG
29 . goat-anti-rabbit HRP / Invitrogen / #31462 / Manufacturer COA reports specific binding to rabbit immunoglobulins, no binding to non immunoglobulin serum proteins, and minimal cross-reactivity with other species
30 . rabbit-anti-phopho-histone H3 (Ser10) / Cell Signaling Technology / #9701 / Manufacturer COA with appropriate detection of phospho site upon induction of phosphorylation, not in its absence
31 . rabbit-anti-cleaved caspase-3 (Asp175) / Cell Signaling Technology / #9661 / Manufacturer COA with appropriate detection of caspase cleavage upon pharmacologic induciton of apoptosis, not in its abssence
32 . Tomm20 (for L1 and DI318 model assays) / Cell Signaling Technology / 42406 / Manufacturer COA reports minimal signal on mouse tissue. Detection of appropriate moleclar weight (western) and cellular localizaton (microscopy) in human tissue
33 . anti-rabbit DyLight405 alpaca antibody / Jackson ImmunoResearch / 611-474-215 / Manufacturer COA reports minimal cross-reactivity with non-rabbit antibodies. Positive signal when used with rabbit primary antibodies
34 . anti-actin hFAB Rhodamine / Bio-Rad / #12004163 / Manufactorer COA reports specific detection of human and rodent actin, and no cross reactivity with other secondaries
35 . anti-sox2 / R&D Systems / MAB2018 / Manufafacturer COA reports specific detection of sox2 in human, mouse, rat cells (western) and tumor specimen microscopy. Negative in non-tumor cells without sox2 expression
36 . anti-oct4 / Cell Signaling Technology / #2750 / Manufacturer COA with appropriate staining of human testicular cancer, negative in normal testes. Western with detection of appropriate sized band
37 . ATP5A-AF647 / Abcam / ab176569 / Manufacturer COA reports appropriate band size detection by western blot, with intensity varying by ATP5A expression
38 . GLUT1-AF647 / Abcam / ab115730 / Manufacturer COA reports specific binding across multiple cell lines, and no binding in knockout cells

Eukaryotic cell lines

Policy information about cell lines and Sex and Gender in Research

Cell line source(s)	1. SB28 (Dr. Hideho Okada, University of San Fransisco). 2. GL261 (Developmental Therapeutics Program, National Cancer Institute). 3. D456 patient-derived xenograft (Dr. Darrel Bigner, Duke University). 4. JX22 patient-derived xenograft (Dr. Jann Sarkaria, Mayo Clinic). 5. CSC293T (Dr. Anita Hjelmeland (co-author)). 6. Human cell lines P3, GG16, BG5 and BG7 are derived from glioblastoma patient biopsies (Dr. Hrvoje Miletic (co-author)). 7. hTERT-immortalized human astrocytes (NHA) were bought from Applied Biological Materials Inc., Vancouver, Canada, Cat# T0281
Authentication	Cell lines have been authenticated by species-specific STR marker profiling. Finger priniting of P3, GG16, BG5 and BG7 cell lines.
Mycoplasma contamination	All cell lines have tested negative for Mycoplasma spp.
Commonly misidentified lines (See ICLAC register)	None of the cell lines in the ICLAC list of misidentified lines.

Animals and other research organisms

Policy information about studies involving animals; ARRIVE guidelines recommended for reporting animal research, and Sex and Gender in Research

Laboratory animals	C57BL/6 wildtype mice (JAX Stock #000664) were purchased as needed from Jackson Laboratory. Tg(CAG- mKate2)1Poche/J (mito::mKate2, stock #032188) mice were purchased from The Jackson Laboratory, and bred in-house. NSG mice were bred in-house. Male and female 4 to 8-week-old mice were used for experiments. 6-week old immunodeficient male and female nude-RNU rats were used in some studies. Mice were fed standard chow (Teklad Global 18% Protein Rodent Diet, cat. No. 2913, Envigo) and filtered water ad libitum, housed in forced/filtered air isolator cages containing up to 5 mice, with 12 hour light/dark cycles; temperature is maintained at 20-26□C and humidity at 30-70%. Immunodeficient nude-RNU rats of both sexes, bred in house (Bergen, Norway) were fed a diet containing standard pellets (Sniff, V1536-000), and had access to water ad libitum, and were housed in filtered air isolator cages (Allentown type IV (Rat 1800), HEPA

	filter) with 12 hour light/dark cycles, 21EC and ca. 45% humidity.
Wild animals	This study did not involve wild animals.
Reporting on sex	This study did not analyse sex-based differences. A combination of male and female animals were utilized for all experiments, with the exception of in vivo tumor initiation studies. The reason for the latter was that we were limited in sorted cell number and our prior research indicated that tumor penetrance is overall higher in males, thus requiring fewer cells for the experiment.
Field-collected samples	This study did not involve any field collection.
Ethics oversight	All the studies were approved by the Cleveland Clinic Institutional Animal Care and Use Committee or by the Norwegian National Animal Research Authority. Study approval number for Cleveland Clinic is 2019-2179.

Note that full information on the approval of the study protocol must also be provided in the manuscript.

Flow Cytometry

Plots

Confirm that:

☒ The axis labels state the marker and fluorochrome used (e.g. CD4-FITC).

☒ The axis scales are clearly visible. Include numbers along axes only for bottom left plot of group (a 'group' is an analysis of identical markers).

☒ All plots are contour plots with outliers or pseudocolor plots.

☒ A numerical value for number of cells or percentage (with statistics) is provided.

Methodology

Sample preparation	In vivo experiments: At experiment endpoint, mice were euthanized, and resected tumors or the contralateral hemisphere were digested with 1 mg/mL collagenase IV (StemCell Technologies) and 1 mg/mL DNAse I (Roche) for 15 minutes at 37°C. Samples were strained trough a 100 µm strainer (Fisherbrand) and washed with PBS prior to staining. In vitro experiments: Co-cultures of primary cells + mouse GBM cell lines were harvested by 5 min of incubation with Accutase, and washed with PBS prior to staining. Human cell line samples were seeded according to the experimental set up and attached on Matrigel in NB medium with additives. At harvest, growth medium from the samples was removed and cells were detached using pre-warmed Accutase (AC) (37 degrees C) for approx. 5 min. AC was inactivated with medium from the corresponding sample and single cell suspension (SCS) was made. Samples were then sifted through a 40 um filter and pelleted in a pre-cooled centrifuge (4 degrees C). Supernatant was removed and samples were resuspended in pre-cooled 1x PBS (4 degrees C) and kept on ice until flow cytometry. Cocultures of human cell line spheroids and fetal rat brain organoids (FRBO) were harvested after 72 hours (immediately following final imaging). To secure adequate cells for practical lab work and later flow analysis, provide a mean estimate of mitochondria transfer across all samples as well as an equal number of cells in each flow sample, all cocultures from corresponding conditions were pooled in labelled 1,5 ml Eppendorf tubes. Spheroid/FRBO aggregates precipitated spontaneously. Growth medium was removed before adding pre-warmed Trypsin (37 degrees C) for approx. 5 min with regular vortexing. Trypsin was inactivated with medium from the corresponding sample and SCS was made by slight vortexing. To preserve cell numbers, samples were not filtered. Pelleting was done in a pre-cooled centrifuge (4 degrees C). Supernatant was removed and samples were resuspended in pre-cooled 1x PBS (4 degrees C) with a volume corresponding to three flow samples. Finally, the samples were distributed into three equal volumes and kept on ice until flow cytometry. Brain/Tumor tissue was harvested from immunodeficient nude-RNU rats. Half the tumor (approx. 400-500 mg) was fixed for imaging analysis while the other half was dissociated into SCS using Macs Neural Dissociation Kit (P) from Miltenyi Biotec (130-092-628). All steps were done according to the manufacturers protocol. After SCS, samples were resuspended in pre-cooled 1x PBS (4 degrees C) and kept on ice until flow cytometry. For staining, washed cells (in PBS) were stained with LIVE/DEAD™ Fixable Blue Dead Cell Stain Kit (Thermo Fisher Scientific) for 10 minutes on ice, and then washed with PBS+2% BSA, treated with 1:50 diluted FcR blocking reagent (Miltenyi Biotec) for 15 minutes on ice and then stained with any indicated surface antibodies in PBS+2% BSA. Samples requiring intracellular antibody staining were fixed 30 min to overnight with eBioscience FoxP3 Transcription Factor Fixation Kit, and then stained with intracellular antibody cocktail.
Instrument	BD LSR Fortessa
Software	Data collection: FACS Diva v9.0 or v8.0 Data analysis: FlowJo software (BD Biosciences, v10.7.2)
Cell population abundance	-Purity check of sorted samples was performed by reloading the sorted fractions to Aria II sorter and by confirming their fluorescence profile. -Gene expression analysis was used as additional confirmation in sort experiment used for RNAseq. -Purity of sorted astrocytes was >95%. Purity of sorted mouse tumor cell lines overall was >95% (with regard to astrocyte contamination). Purity of mKate negative mouse tumor cell lines (i.e. cells that did not uptake astrocyte mitochondria in co-culture) was >95%. Purity of mKate positive mouse tumor cell lines (i.e. cells that did uptake astrocyte mitochondria in co-culture varied from 30-45%. -Purity of sorted mito::mCherry positive and negative human GBM cells from co-cultures was 80-95% -Sample purity was determined by internal, technical controls for each and every experiment, thereby providing a continuous surveillance of sample fluorescence and quality. The same cells used for controls and experimental groups were

simultaneously seeded to provide single fluorescence samples. These samples were used to control for fluorescent cross-contamination and for compensation under analysis. Corresponding WT cells were used as negative controls to gauge autofluorescence and provide a non-fluorescent comparison for compensation, gating and analysis purposes. For experiments using fetal rat brain organoids (FRBO), non-transduced wild-type organoids were seeded and analyzed in parallel as negative controls. For animal experiments, WT and fluorescent cells lines corresponding to the tumor were used as controls.

Gating strategy

-FSC-A/SSC-A plots were used to gate on cells, and FSC-A/FSC-H plots were used to determine the single cells and live staining was used to exclude the dead cells. For the main readout of mKate2 or mito::mCherry fluorescence positivity, background signal was determined either by using matching tumor cells that had been co-cultured with wildtype (fluorophore negative) donor cells, or obtained from intracranial tumors implanted in wiltype mice.
-The gating strategy was developed to quantify mitochondria transfer, as defined by GFP+/DsRed- events becoming GFP+/DsRed+ events. Initially, technical controls were used for making a fluorescent-specific matrix to compensate for possible spillover which could affect results. Gates were then created by identifying live cells, single cells and GFP+/DsRed- events using the GFP-/DsRed+ control sample. These gates were applied to the group as a whole, before using the GFP+/DsRed- control sample to make a final gate defining GFP+/DsRed+ events. This gate was applied to the group as a whole, thereby creating a common gating tree for all experimental and control samples indicating live cells, single cells, GFP+/DsRed- events and GFP+/DsRed+ events. The latter was defined as total mitochondria transfer, and the frequency of parent statistic was used in subsequent analyses. In parallel, other internal parameters were analyzed to check individual experimental quality, including live cells and GFP+/DsRed- events (indicating relationship between donors (GFP-/DsRed+) and acceptors (GFP+/DsRed-) in culture). The said strategy was used on all experiments without exception.
-For GFP+/DsRed- events the boundary between “positive” and “negative” was defined at or around 103 when utilizing Comp-FITC-A (GFP) on the x-axis and SSC-A on the y-axis.
- For GFP+/DsRed+ events the boundary between “positive” and “negative” was defined by the lowest threshold which did not register any GFP+/DsRed+ events in a GFP+/DsRed- control sample. This value was persistently <102 across samples. Such strategy was employed to guarantee that acceptors receiving few mitochondria (DsRed positive in lower end of scale) would still be included for quantification of total mitochondria transfer.
- For live cells and single cells, boundaries between “positive” and “negative” cells were defined using standard gating in a SSC-A/FSC-A plot and FSC-H/FSC-A plot respectively.

☒ Tick this box to confirm that a figure exemplifying the gating strategy is provided in the Supplementary Information.